ISSN 0256-4637
VOLUME 38 NUMBER 3 JULY-SEPTEMBER 2016

Journal of Pure and Applied

Ultrasonics

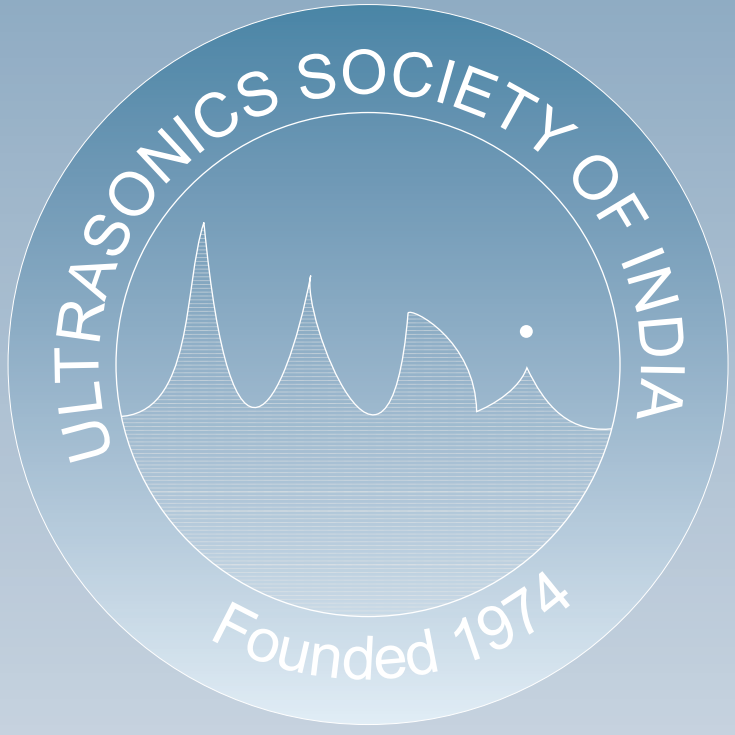

Website : www.ultrasonicsindia.org

A Publication of Ultrasonics Society of India

A Quarterly Publication of Ultrasonics Society of India

Journal of Pure and Applied

Ultrasonics

No. 3	Volume 38	July-September 2016

SUBSCRIPTION (postage paid)

Single	Rs. 550/-	US$ 50/-
Annual	Rs. 2200/-	US$ 200/-
USI *members*	Free	

The submission of papers and all other correspondence regarding the Journal may please be addressed to :

Publication Secretary
Journal of Pure and Applied Ultrasonics
C/o Ultrasonics Society of India
CSIR-National Physical Laboratory
Dr. K.S. Krishnan Road
New Delhi-110012
ultrasonic.devraj@gmail.com
www.ultrasonicsindia.org

ISSN 0256–4637

Journal of Pure and Applied Ultrasonics

VOLUME 38 NUMBER 3 JULY–SEPTEMBER 2016

CONTENTS

(Authors have stated that the papers have not been published elsewhere)

Website : www.ultrasonicsindia.org

A Publication of — Ultrasonics Society of India

J. Pure Appl. Ultrason. 38 (2016) pp. 49-57

Anisotropic divergence controlled ultrasonic transmitter array for three-dimensional range imaging

Sahdev Kumar* and Hideo Furuhashi

Department of Electrical and Electronics Engineering, Aichi Institute of Technology,
1247, Yachigusa, Yakusa-Cho, Toyota, 470-0392, Japan
*E-mail: kumarsahdev42@gmail.com

A simple, cost effective and long-range three-dimensional (3D) measurement system has been developed using ultrasonic sound. The developed system consists of a high-power ultrasonic transmitter array (UTA) and an ultrasonic receiver array (URA). In some particular cases, measurement in wide horizontal plane is required instead of vertical direction. Therefore, anisotropic divergence control has been proposed and successfully controlled maintaining high peak power in the horizontal direction. The characteristics of the UTA are compared with the theory by generating a 40 kHz ultrasonic signal with modulated pulse width 2 ms. The measurable range without divergence control has been obtained over 17 m $\pm$ 0.5 m. Measurable range with anisotropic divergence control has been improved to 16 m $\pm$ 0.5 m on the isotropic divergence control from 14 m $\pm$ 0.5 m at the same divergence angle10°. Awidest view angle has been obtained at 20° with the isotropic divergence control and further improvement in the view angle is observed with the anisotropic divergence control.

Keywords: 3D measurement system, ultrasonic transmitter array, anisotropic directivity, delay time, range image.

Introduction

Recently, three dimensional (3D) positioning, shape and size measurement of an object is one of the thrust areas and efforts are being made to improve the measurable range and resolution. There are several conventional techniques available for 3D object positioning and shape recognition such as stereo camera, laser scanners, pattern projections etc. Ultrasonic image sensor system is also one of such techniques and works on the principle of pulse echo detection method. In spite of low resolution, ultrasonic image sensor system has several advantages over other conventional techniques, such as its effective use in adverse atmospheric conditions[1-6]. A few efforts have been made to improve measurable range such as Tanaka at el. has developed a high power ultrasound source using spark discharge[7]. We have used spread spectrum (SS) pulse compression technique as well as increased the number of transmitting elements. A measurable range up to 6 m has been achieved by the SS pulse compression technique while as measurable range up to 25 m has been demonstrated using ultrasonic transmitter array (UTA) of 12 12 elements and ultrasonic receiver array (URA) of 32 elements[8, 9].

In our experimental results it has been shown that as the number of transmitting elements increases the view angle of object detection reduces[10, 11]. Therefore, to improve the view angle and measurement field, a divergence control on the directivity, such as an isotropic divergence control, had been reported with the improved view angle up to 6°[12,15]. In the isotropic divergence control, the controlled angle is equal in both x and y directions. In some particular cases it is required to measure wide horizontal field and narrow vertical field. Therefore, anisotropic divergence control has been proposed and experimental results were compared with the theoretical calculations[13]. Our experimental results showed that with the isotropic divergence angle control, measurement field increases with an increase in divergence angle but measurable range decreases accordingly[14, 15].

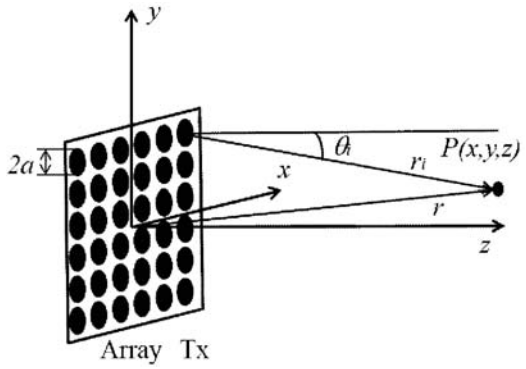

Fig. 1 Coordinate system of calculation.

Theory

Figure 1 shows the coordinate system for the theoretical calculations and Fig. 2 shows the coordinate system of anisotropic divergence control. Considering a number of transmitting element in x, y plane and put at positions P_i (x_i, y_i, 0); the sound pressure at an observation point is obtained by Eq. (1) as follows[13].

$$|p(x,y,z)| = D(\theta_i)A\frac{1}{r} \left| \sum_i^n \exp\left\{-\frac{2}{\lambda}(x_i \sin\theta_x + y_i \sin\theta_y + \frac{x_i^2}{2L_x} + \frac{y_i^2}{2L_y})\right\}\right| \quad (1)$$

Here, A is the amplitude of the sound pressure of one transmitter; r is the distance between the origin, i.e., the center of the array and the observation point *P (x, y, z)*. The angles between the vector $\overrightarrow{OP}$ and the *yz* plane & *xz* planes are θ_x and θ_y, respectively. The $D(\theta_i)$ are the directivities of the UTA elements. The L_x and L_y are the distances between the center of the UTA and center of the divergence angle and calculated by the following Eq. (2) and Eq. (3)

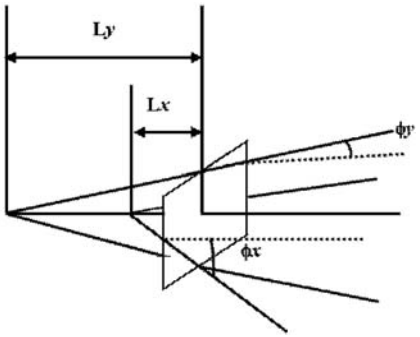

Fig. 2 Coordinate system of anisotropic divergence calculation.

$$L_x = \frac{(n-1)d}{2\tan\phi_x} \quad (2)$$

$$L_y = \frac{(n-1)d}{2\tan\phi_y} \quad (3)$$

Here, θ_x and θ_y are the angles of the divergence in *x* and *y* directions, *n* is number of ultrasonic transmitter elements in the arrays, *d* is inter element spacing. In this case time delay applied to each element is calculated by Eq. (4), where, *v* is the wave velocity.

$$\Delta\tau_d \approx (\frac{x_i^2}{L_x} + \frac{y_i^2}{L_y})\frac{1}{2v} \quad (4)$$

Ultrasonic Transmitting and Receiving System

(a) Ultrasonic transmitting system

A photograph of the developed UTA sound source is shown in Fig. 3 that consists of 12 × 12 arrays of transmitting elements; a device T4010B4 (Nippon Ceramic Co. Ltd). This device has the beam directivity 100° (-6dB full angle) and resonant frequency of 40 kHz. Each device can be operated at sound pressure 121.5 dB, input voltage 10 Vrms at a distance 30 cm with the ultrasonic oscillation frequency 40 kHz. The devices are arranged in such a way that they maintained inter element space of 1 cm. A schematic block diagram of the UTA transmitting system is shown in Fig. 4. The signal applied to each transducer element is controlled by field programmable gate array (FGPA) (XILINXXC6SLX150) boards with a 50 MHz, clock

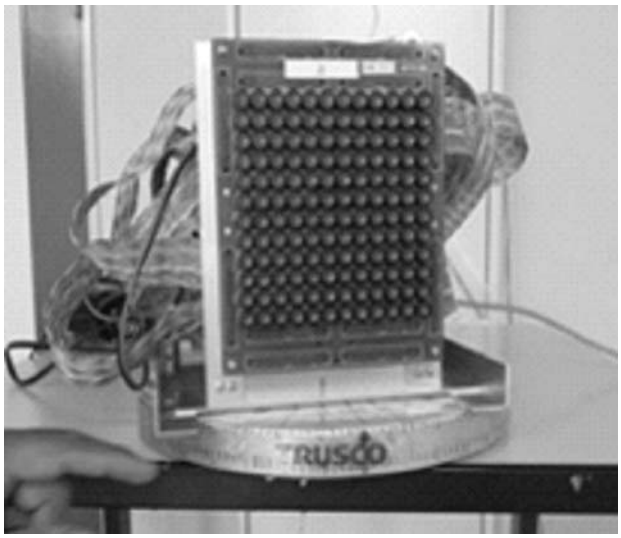

Fig. 3 Developed ultrasonic transmitter array

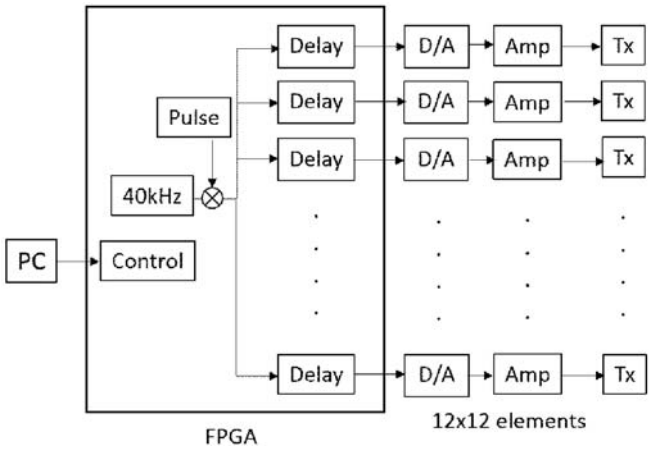

Fig. 4 A schematic block diagram of the ultrasonic transmitting system

signal in the form of modulated signal of 40 kHz frequency with a 2 ms pulse width and 400 ms pulse repetition period is stored in a ring buffer. Each board can control 36 transducer elements; thus, four boards are used to control the 144 transducer elements. One of them is the master board and other three boards are the slave boards. Master board feed the amplitude-modulated digital signal to all the three slave boards. The time delays with rounded off value to 1 s are calculated by a personal computer and sent to the FPGA boards.Thus delayed signals are converted from analog to digital and *vice versa* by D/A converters AD5415 (a 12-bit, dual-channel, current output digital-to-analog converter) at a sampling rate of 1 s. The transducers are operated with a maximum input of 30 V_{pp} (peak to peak).

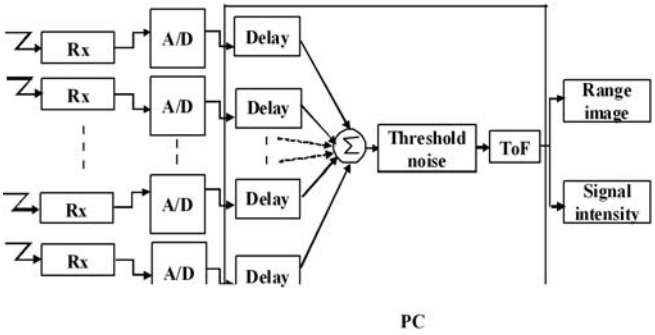

Fig. 5 A schematic block diagram of the ultrasonic receiving system

(b) Ultrasonic receiving system

The URA receiving system consists of 32 receivers and Omni-directional SP0103NC3-3 (6.15 mm (length) × 3.76 mm (width) × 1.45 mm (height) devices are being used for the receiver. Fig. 5 shows the schematic block diagram of the ultrasonic receiving system. Ultrasonic sound, transmitted by the UTA is received by the URA after its reflection from a plastic board of 30 cm width and 80 cm length. The A/D converter device TSM - 372012 (Interface Corporation) converts the received nalogue signal into digital form. The signal conversion time from analog to digital is 2.5 s with a 12 bits resolution. The outputs of the developed ultrasonic image sensor system are shown in two windows one as range image and another as signal intensity of the target object after delay-and-sum (DAS) operations on the processed data through personal computer.

Experimental Set-up

The experimental set-up is depicted in Fig. 6. The transmitted signal is received by a sensor at 5 m away from the UTA. The height of UTA and sensor is 1.5 m above the ground level. The sensor is calibrated at the ultrasonic frequency by a system using a ¼-inch free-field response microphone (46BE; frequency range 4 Hz-80 kHz, dynamic range 36 dB-157 dB, a data acquisition module (USB-4431; 24-Bit Analog I/O, sampling rate of 102.4 kS/s, and a sound measurement analyzer. A device MA40S4R is being used as a sensor which has a nominal frequency of 40 kHz and beam width of 80°. The experiment is first aligned by obtaining the maximum amplitude of the direct received signal at the same horizon. After initialization the experimental conditions, divergences are input through personal computer and time delay is automatically calculated by the system. Maximum peak to peak voltage is measured, by manually rotating the UTA in the horizontal plane

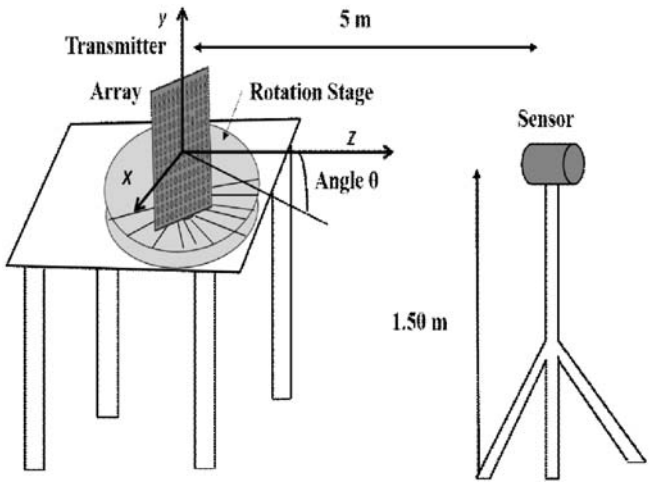

Fig. 6 Experimental set-up.

with the azimuthal angle from 0° to 90° with 2° steps. The ultrasonic wave velocity is considered 345 m/s at room temperature 23°C for this experiment.

Experimental Results and Discussion

(a) Sound pressure level at different anisotropic divergences

Figure 7 shows the sound pressure level (SPL) of the UTA. The SPLs with isotropic divergence, *i.e.* $\phi_x = \phi_y$ are shown by the circles. The SPLs of a single ultrasonic transmitter (SUT) and UTA without divergence control are shown by straight dash-dotted line and narrow dotted line respectively. The SPL with vertical divergence angle, ϕ_y=0° and ϕ_y=5° are shown by the circles and triangles, respectively. The SPL with ϕ_y=5° is less than ϕ_y=0° at the equal interval, however, decreases significantly with the isotropic divergence. Therefore, high peak sound pressure can be maintained with the controlled vertical divergence angles. The SPLs with ϕ_x=0°, 5°, 10° and 15° for ϕ_y = 5° are obtained as 125.3 dB, 124.8 dB, 119.9 dB and 115 dB, respectively.

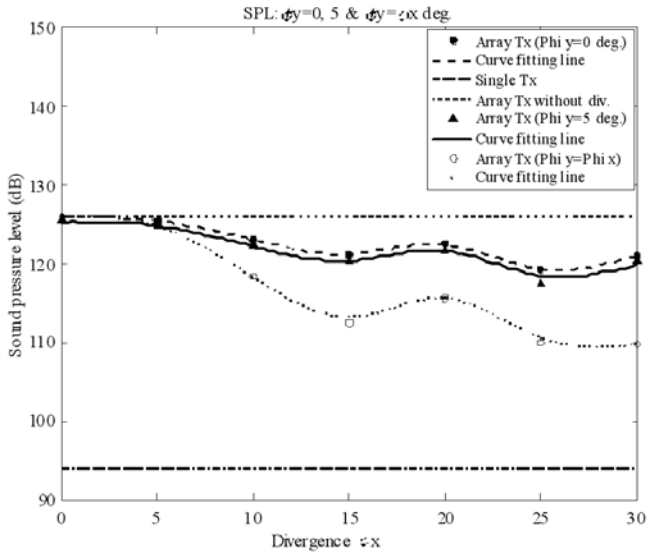

Fig. 7 Sound pressure level at different divergence angles.

Figure 8 shows the directivity without divergence ϕ_x= ϕ_y=0° and and obtained using Eq. (1) under the following consideration $\sin\theta_x\, x_i + \sin\theta_y\, y_i$=0 on the *z* axis and ($\theta_x$= θ and θ_y = 0). Figures 9 (a) - (c) show the directivities of the UTA when divergence ϕ_x = 5°, 10° and 15°; ϕ_y = 5°, respectively. The dots show the experimental data and smooth line shows the simulation results. Applying the half width at half maximum (HWHM) on the

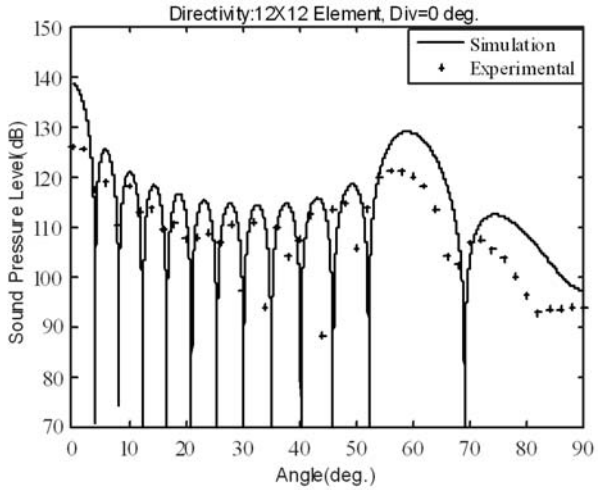

Fig. 8 Directivity of 12×12 ultrasonic transmitter array (UTA) without divergence.

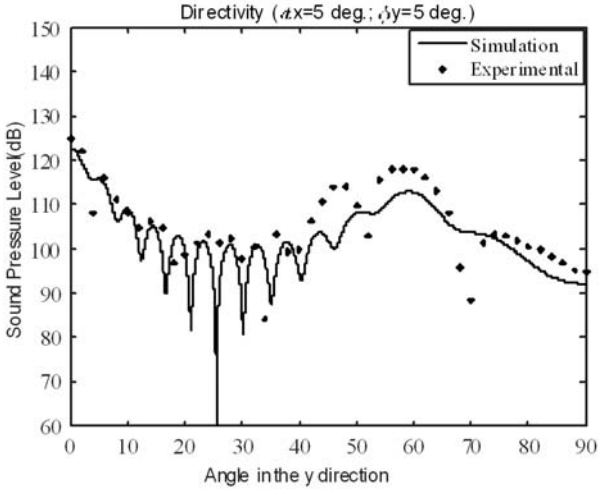

Fig. 9(a) Experimental: Dots; Theoretical: Solid line ϕ_x = 5°, ϕ_y = 5° and θ = 0°.

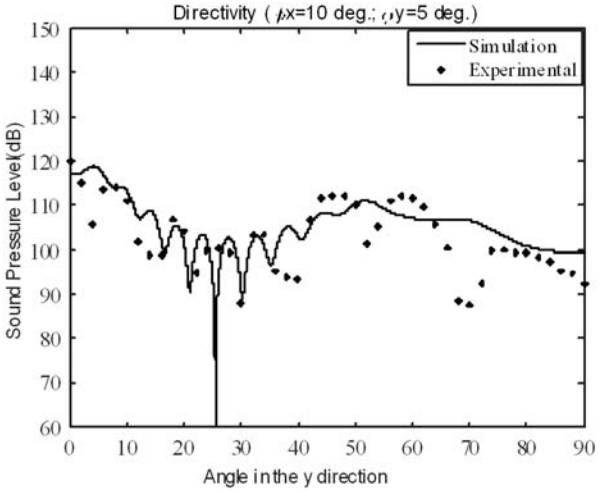

Fig. 9(b) Experimental: Dots; Theoretical: Solid line ϕ_x = 10°, ϕ_y = 5° and θ = 0°.

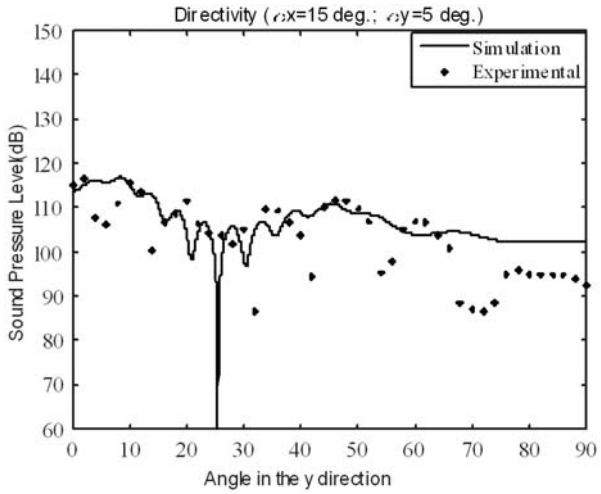

Fig. 9(c) Experimental: Dots; Theoretical: Solid line $\phi_x = 15°$, $\phi_y = 5°$ and $\theta = 0°$.

experimental data, HWHM measured 5°, 10° and 15° according to the applied horizontal divergence on the system.

(b) Measurable range

Figure 10 shows the measurable range at different divergence angles obtained using a plastic board (30 cm width × 80 cm height). Transmitted signal is received after reflection from the plastic board using the UTA and the ultrasonic single receiver (USR). The USR is placed adjacent to the UTA at 30 cm distance. A distance of the plastic board from the transceiver (Tx/Rx), until reflected ultrasonic signal was clearly detected from the back ground noise is considered as its measurable range. The developed system works on the ultrasonic pulse echo detection method and received signal amplitude "A" is directly proportional to the following quantity given by Eq. (5)[11].

$$A \propto \frac{e^{-2\gamma r}}{r^2} \tag{5}$$

Where, r is the distance between the ultrasonic transceiver and the object and γ denotes the absorption coefficient. Considering the measurable range of the SUT and the UTA as $r`$ and $r``$ then a relationship can be formulated as Eq. (6)

$$\frac{e^{-2\gamma r`}}{r`^2} = k\frac{e^{-2\gamma r``}}{r``^2} \tag{6}$$

Here, k is the ratio of sound pressure transmitted by the UTA to that of SUT and calculated as 34.7, 19.7 and 11.2 when $\phi_x = 5°$, 10° and 15°; $\phi_y = 5°$, respectively. Theoretical measurable ranges for different k are denoted by dashed, dash-dotted and smooth black line and calculated at γ=0.12/m according to Eq. (6). A measurable range without divergence angle control is 17 m $\pm$ 0.5 m. The measurable ranges for isotropic divergence angle control *i.e.* $\phi_x = \phi_y = 10°$ and anisotropic divergence angle control $\phi_x = 10°$; $\phi_y = 5°$ are 14m $\pm$ 0.5 m and 16 m $\pm$ 0.5 m have been obtained. Figure 11 shows the signal intensity of the URA at divergence angle ϕ_y = 0° & 5° when object is at the angular direction $\theta = 0°$. The circles and the triangles are the experimental results. The signal intensity is lower at vertical divergence angle $\phi_y = 5°$ in comparison to $\phi_y = 0°$.

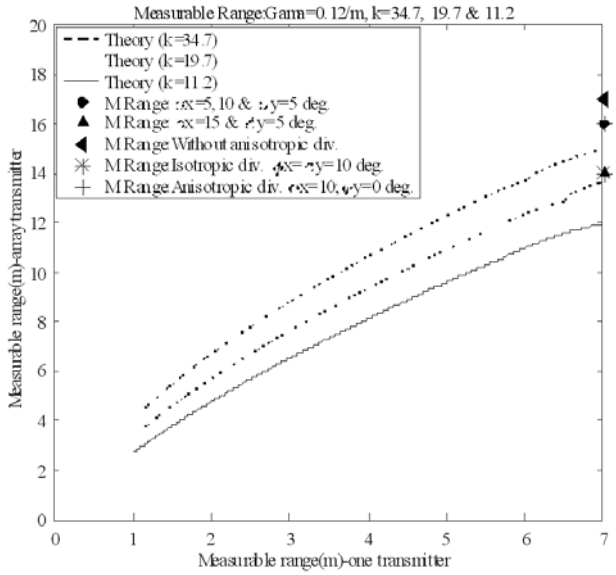

Fig. 10 Theoretical and experimental results for measurable range.

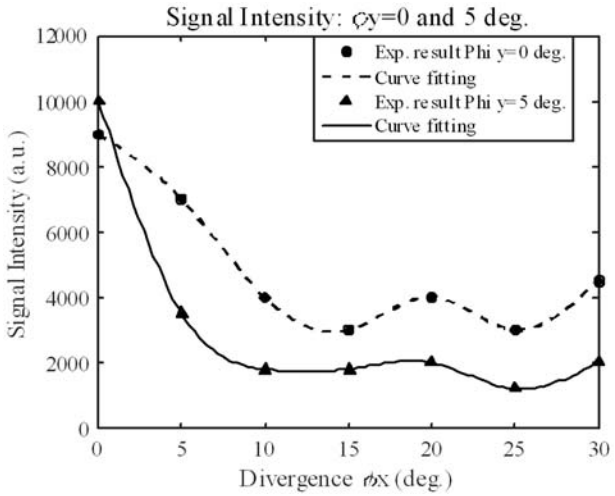

Fig 11 Signal intensity of the ultrasonic receiver array at ϕ_x = 0° & ϕ_y = 0° and ϕ_x = 0° & ϕ_y = 5° and $\theta = 0°$.

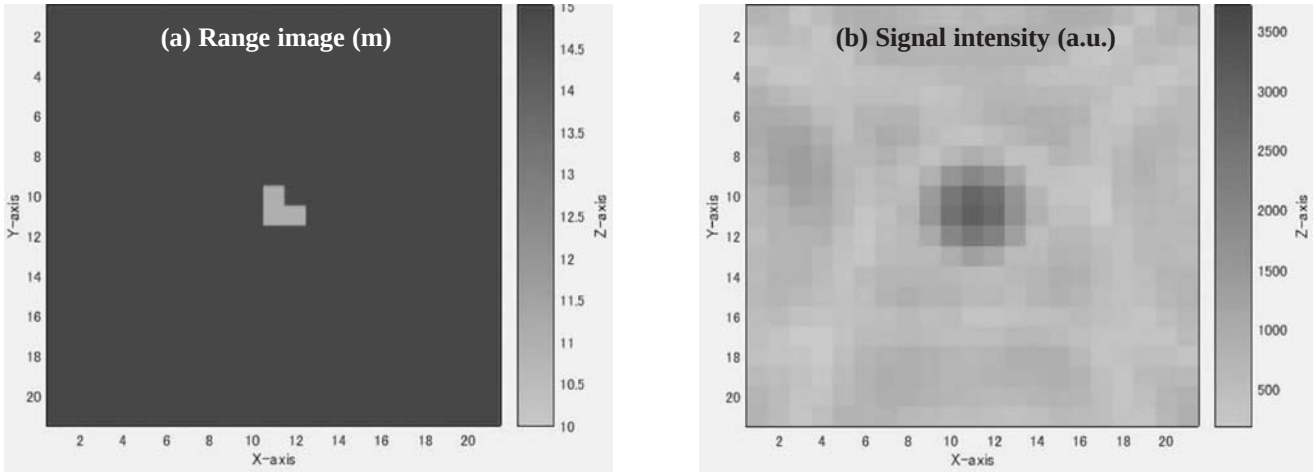

Fig 12 Range image and signal intensity using the UTA and the URA for an object placed at 12 m away in θ=0° direction and divergence angles are: ϕ_x=5°, ϕ_y=5°, x & y axis are 5°/div., and z axis shows the distance between transceiver and object with corresponding signal intensity.

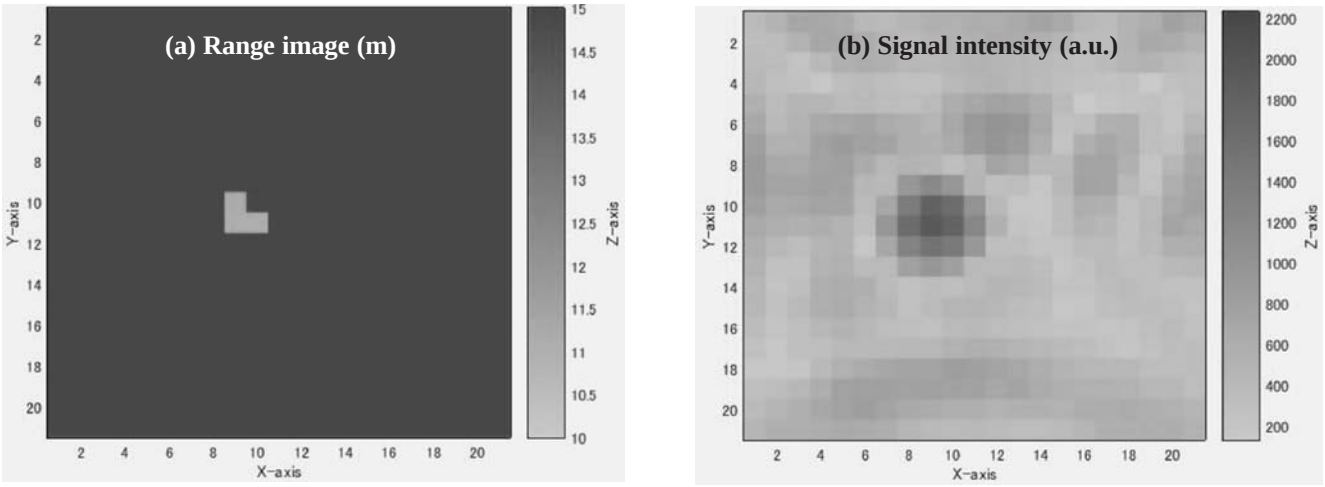

Fig. 13 Range image and signal intensity using the UTA and the URA for an object placed at 12 m away in θ=10° direction and divergence angles are: ϕ_x=5°, ϕ_y=5°, x & y axis are 5°/div., and z axis shows the distance between transceiver and object with corresponding signal intensity.

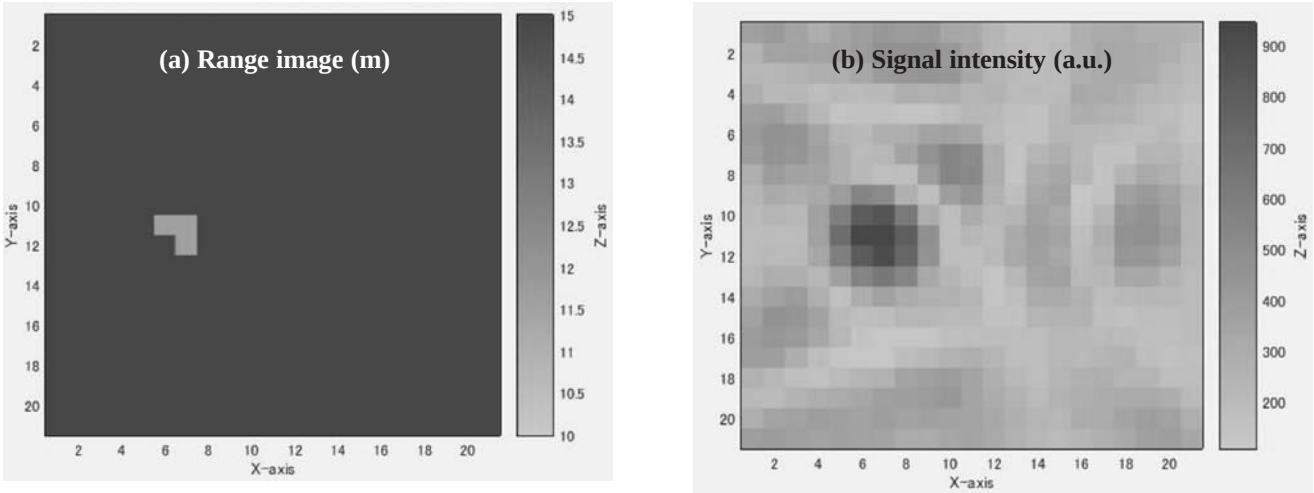

Fig. 14 Range image and signal intensity using the UTA and the URA for an object placed at 12 m away in θ=20° direction and divergence angles are: ϕ_x=5°, ϕ_y=5°, x & y axis are 5°/div., and z axis shows the distance between transceiver and object with corresponding signal intensity.

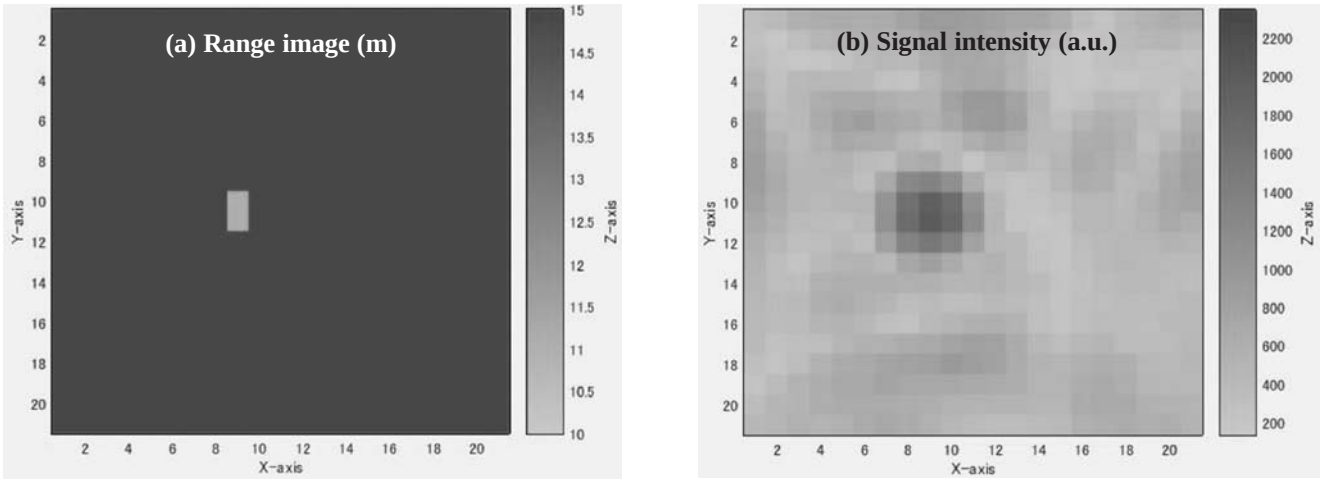

Fig. 15 Range image and signal intensity using the UTA and the URA for an object placed at 12 m away in θ=10° direction and divergence angles are: ϕ_x=10°, ϕ_y=5°, x & y axis are 5°/div., and z axis shows the distance between transceiver and object with corresponding signal intensity.

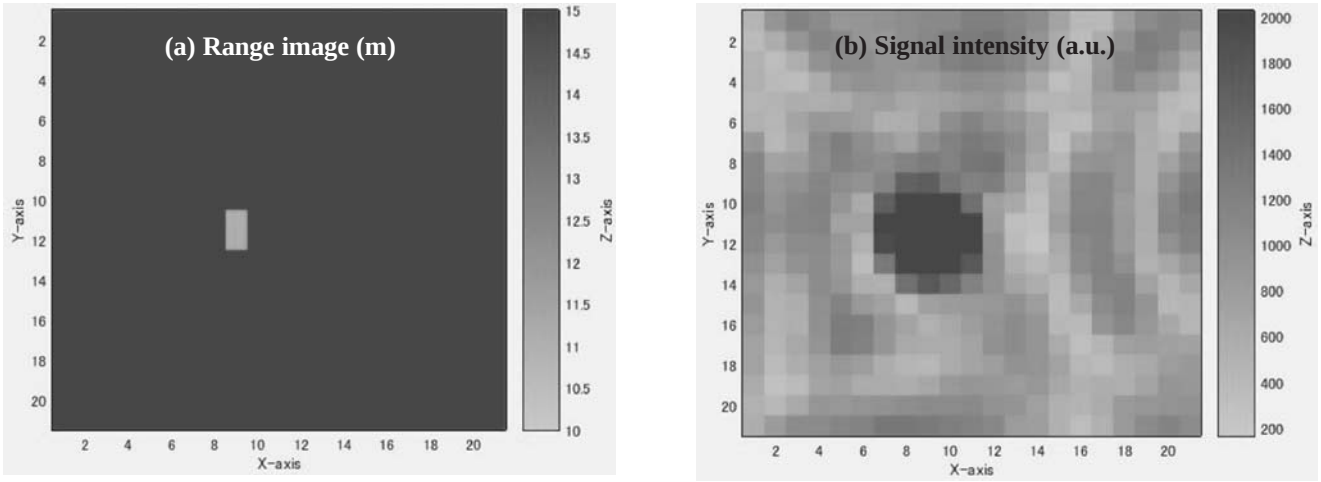

Fig. 16 Range image and signal intensity using the UTA and the URA for an object placed at 12 m away in θ=10° direction and divergence angles are: ϕ_x=20°, ϕ_y=5°, x & y axis are 5°/div., and z axis shows the distance between transceiver and object with corresponding signal intensity.

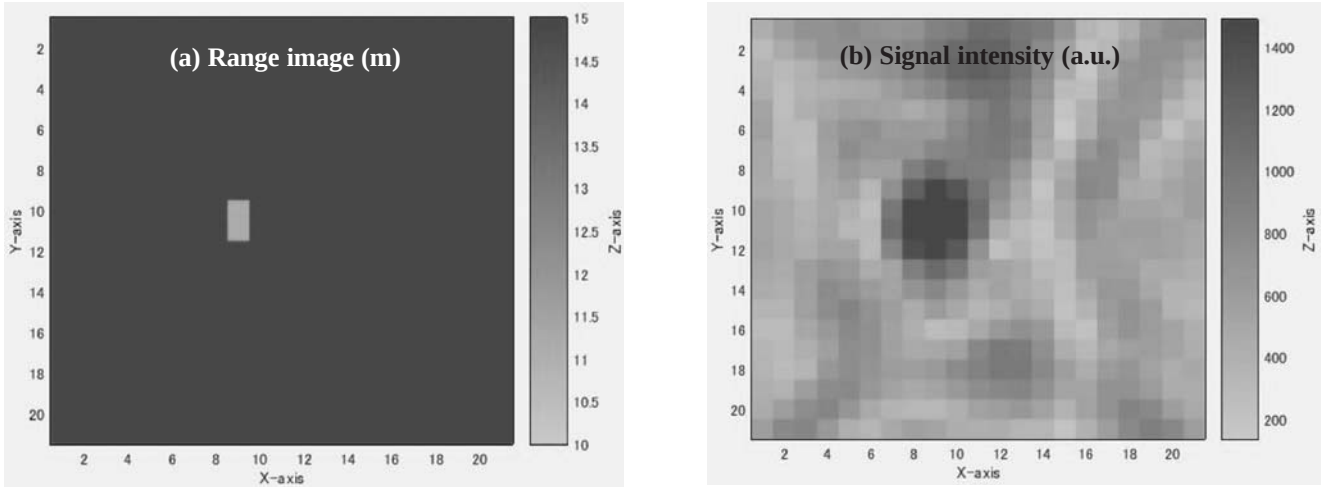

Fig. 17 Range image and signal intensity using the UTA and the URA for an object placed at 12 m away in θ=10° direction and divergence angles are: ϕ_x=30°, ϕ_y=5°, x & y axis are 5°/div., and z axis shows the distance between transceiver and object with corresponding signal intensity.

Figure 12 (a) is the range image of an object placed at 12 m away from the UTA, when $\phi_x = 5°$; $\phi_y = 5°$ and the object is at $\theta = 0°$ direction; Figure12 (b) shows the corresponding reflected ultrasonic signal intensity distribution obtained by the DAS operation. Figure 13(a) shows the range image of an object placed at 12 m away from the UTA, when $\phi_x = 5°$; $\phi_y = 5°$ and the object is at $\theta = 10°$ direction. Figure 13(b) shows the corresponding reflected ultrasonic signal intensity distribution obtained by the DAS operation. Figure 14 (a) shows the range image of an object placed at 12 m away from the UTA, when $\phi_x = 5°$; $\phi_y = 5°$ and the object is at $\theta = 20°$ direction. Figure 14 (b) shows the corresponding reflected ultrasonic signal intensity distribution obtained by the DAS operation. Figure 15 (a) shows the range image of an object placed at 12 m away from the UTA, when $\phi_x = 10°$; $\phi_y = 5°$ and the object is at $\theta = 10°$ direction. Figure 15(b) shows the corresponding reflected ultrasonic signal intensity distribution obtained by the DAS operation. Figure 16 (a) shows the range image of an object placed at 12 m away from the UTA, when $\phi_x = 20°$; $\phi_y = 5°$ and the object is at $\theta = 10°$ direction. Figure 16(b) Shows the corresponding reflected ultrasonic signal intensity distribution obtained by the DAS operation. Figure 17 (a) shows the range image of an object placed at 12 m away from the UTA, when $\phi_x = 30°$; $\phi_y = 5°$ and the object is at $\theta = 10°$ direction. Figure 17(b) Shows the corresponding reflected ultrasonic signal intensity distribution obtained by the DAS operation.

Detection of object position

The distribution of the maximum signal intensity in the range image data was calculated at the time when the correlated signal reached to its maximum value. The signal intensity and the range images are displayed in 21 × 21 pixels constructed by using Matlab and Simulink. The total field of view angle of the UTA in *x* and *y* directions is 105° × 105°. For example an object placed at 12 m in the direction $\theta = 0°$ and divergence angles of signal transmission are $\phi_x = 5°$ and $\phi_y = 5°$ from the UTA, its range image is detected at the center position of the 21×21 pixels as given by $0° \times \frac{21 \text{ pixels}}{105°} + \frac{21 \text{ pixels}}{2} = 11^{th}$ pixel. Therefore pixel point (11, 11) is in the center. The image was successfully obtained at the center as shown in Fig.12 (b). The z-axis in the Fig. 12 (a) shows the distance between UTA and the object by matching the color of the image obtained with the z-axis color bar. The position coordinate of the image is (0, 0, 12 m) and experimentally detected position coordinate is (0, 0, 11.6 m) on the z-axis as shown in Fig.12 (a). When the object is placed at 12 m in the direction $\theta = 10°$ and divergence angles of signal transmission are $\phi_x = 5°$ and $\phi_y = 5°$ from UTA, its range image is detected at 2 pixels sifted left from the center position of the 21×21 pixels given by $-10° \times \frac{21 \text{ pixels}}{105°} + \frac{21 \text{ pixels}}{2} = 9^{th}$ pixel. The pixel point (9, 11) is shown in Fig.13 (b). The range image position coordinate is (–2, 0, 12). The angular view resolution 5°/pixel and the object is experimentally detected at position coordinate (–10°, 0, 11.6 m) on the z-axis as shown in Fig.13 (a). Similarly, the range image coordinate of an object placed at 12 m in the direction $\theta = 20°$ and divergence angles are $\phi_x = 5°$ and $\phi_y = 5°$ from the UTA is (–4, 0, 12) and its image detected at the pixel point (7, 11) as shown in Figs. 14 (b) and 14 (a). The object is experimentally detected at position coordinate (–20°, 0, 11.6 m) on the z-axis. The Range image coordinates of an object placed at 12 m in the direction $\theta = 10°$ and divergence angles of signal transmission are $\phi_x = 10°$ and $\phi_y = 5°$, $\phi_x = 20°$ and $\phi_y = 5°$, and $\phi_x = 30°$ and $\phi_y = 5°$ from the UTA is (–2, 0, 12) for each case and their image detected at the pixel point (9, 11) as shown in Figs. 15 (b), 16 (b) and 17 (b), respectively. The position coordinates of the object experimentally detected are (–10°, 0, 11.7 m), (–10°, 0, 11.7 m), and (–10°, 0, 11.5 m), respectively. The negative signed angle shows that the object is in the left side with respect to the angle $\theta = 0$ odirection from the UTA.

Further, pixel measurement error in considered 1×1 pixel for the variation in the view angle of 5°. An object range image resolution depends on uncertainties in the ultrasonic pulse width, ultrasonic speed in open air, object size and the object distance from the UTA as :

$$\Delta z = \left(\frac{\text{Pulse width (s)} \times \text{Wave speed (m/s)}}{2} \right) + \text{positioning error (m)} \Rightarrow \frac{.002 \times 345}{2} + 0.20 \text{ and calculatedas } \Delta z = 0.55$$

m for ultrasonic pulse width 2 ms, pulse wave speed 345 m/s and the object positioning error 0.20 m. Itis in good agreement with experimental error of $\pm$0.50 m.

Conclusion

A long-range 3D measurement system has been developed and directivity is successfully controlled by controlling the anisotropic divergence angles of the transmitted signal of UTA. Although, measurable range decreases as the isotropic divergence control angle, *i.e.*,

$\phi_x = \phi_y$ increases and sound pressure decreases significantly. Measurable range of the system with anisotropic divergence angle control has been improved over the isotropic divergence angle control by more than 2 m $\pm$ 0.5 m. Measurable range without divergence angle control is 17 m $\pm$ 0.5 m with a very narrow view angle. The most wide view angle is obtained for isotropic divergence angle 20o and further improvement in the view angle is observed with the anisotropic divergence angle controlled system. This 3 D imaging system that comprising the UTA and the URA clearly detects the object position in the different directions maintaining high peak sound pressure in the divergence angle direction, that results improvement in measurable range and view angle. Our experimental results are in agreement with the theoretical calculations and good control on directivity has been obtained with the anisotropic divergence control angle.

Acknowledgements

This study has received a grant of JSPS Research Institute expenses 15K05879 and we thankfully acknowledge the financial support received from Rotary Yoneyama Memorial foundation, Japan. SK is grateful to the Prof. Masakazu Mori, Dr. Brahm Pal Singh and Ms Aishwarya Singh for their valuable suggestions, discussions and assistance for the entire work.

References

1 **Hickling R.** and **Marin S.P.**, The use of ultrasonics for gauging and proximity sensing in air, *J. Acoust. Soc. Am.* **79**(4) (1986) 1151-1160. http://dx.doi.org/10.1121/1.393387.

2 **Turnbull D.H.** and **Foster F.S.**, Beam Steering with Pulsed Two-Dimensional Transducer Arrays, *IEEE Transac. Ultrason. Ferroelectrics and Frequency control*, **38**(4) (1991) 320-333.

3. **Furuhashi H., Valle J., Uchida Y.** and **Shimizu M.**, Imaging sensor system using dispersed ultrasonic array. *Proc. Int. Conf. on Control, Automation and System* (ICCAS 2007), FEP- **35** (2007) 2385-2388.

4. **Furuhashi H., Uchida Y.** and **Shimizu M.**, Imaging sensor system using rectified delay-and-multiply operations with an ultrasonic array, *Proc. IEEE, IECON, IEEE Explore* (2008) 1891-1895.

5 **Furuhashi H., Uchida Y.** and **Shimizu M.**, Imaging sensor system using composite ultrasonic array, Sensors 2009, *IEEE Explore* (2009) 1467-1472.

6 **Furuhashi H., Kuzuya Y., Uchida Y.** and **Shimizu M.**, Three dimensional imaging sensor system using an ultrasonic array sensor and a camera. Sensors 2010, *IEEE Explore* (2010) 713-718.

7 **Tanaka T., Lee S., Uno M., Inoue K., Aoyagi S., Yamashita K.** and **Okuyama M.**, Improvement of ultrasonic micro array sensor using the amorphous fluorocarbon polymer film, *Transac. Inst. Electr. Eng. Jpn: Publ. Sens. Micromach. Soc.*, **127**(1) (2007) 7-13.

8 **Furuhashi H., Kumar S.** and **Shimizu M.**, Signal processing of a 3D ultrasonic imaging sensor that uses the spread spectrum pulse compression technique, Lecture notes in information technology, *Proc. Int. Conf. on Future Information Technology and Management Science & Engineering, FITMSE* 2012, **14** (2012) 145-150.

9. **Kumar S.** and **Furuhashi H.**, Long-range measurement system using ultrasonic range sensor with high-power transmitter array in air. *Ultrasonics*, **74** (2017) 186-195; DOI:10.1016/j.ultras.2016.10.012.

10 **Kumar S., Wei Q.** and **Furuhashi H.**, Characteristics of High-Power ultrasonic array transmitter in air, *Proc. IEEE 2015, Int. Conf. on Recent Developments in Control, Automation and Power Engineering, RDCAPE* 2015, (2015) 209-213. DOI: 10.1109/RDCAPE.2015.7281397.

11 **Kumar S., Ichi K.** and **Furuhashi H.**, Theoretical investigation of high-power ultrasonic array transmitter for a range sensor in air, *Proc. IEEE, Int. Conf. on Industrial Technology ICIT 2013, IEEE Explore* (2013) 1190-1195, DOI:10.1109/ICIT.2013.

12 **Kumar S., Ichi K.** and **Furuhashi H.**, Theoretical investigation of divergence control of directivity of an ultrasonic transmitter array, *SICE Annual Conf.-2013, Abstract SuCT*2.1 (2013) 803-807.

13 **Kumar S., Ichi K.** and **Furuhashi H.**, Theoretical investigation of an ultrasonic array transmitter with anisotropic directivity, *Proc. Int. Conf. on Sensor Device Technologies and Applications SENSOR DEVICES*-2013 (2013) 131-134.

14 **Kumar S.** and **Furuhashi H.**, Development of a High-Power array transmitter for an ultrasonic range sensor in the air, *Proc. Int. Conf. Ultrasonics*-2016, P-42 (2016) 309-310.

15 **Kumar S.** and **Furuhashi H.**, Improved 3-D measurement field of an object in air by controlling the divergence of the array transmission system. Ultrasonics submitted.

J. Pure Appl. Ultrason. 38 (2016) pp. 58-64

Weld defects studies of EN-8 mild steel by non-destructive techniques

S.V. Ranganayakulu[1*], Samrat Goud Burra[1], B. Ramesh Kumar[2] and B. Sreenivasa Verma[3]

[1]Centre for Non Destructive Evaluation, Guru Nanak Institutions,
Technical Campus, Ibrahimpatnam-501506, India
[2]Institute for Plasma Research, Bhat, Gandhinagar-382428, India.
[3]Dept. of Mechanical Engineering, CMRIET, Hyderabad-501401, India
*E-mail: nayakulu@rediffmail.com

The present paper reports the weld quality evaluations carried on EN-08 mild steel samples fabricated with Tungsten Inert Gas (TIG) welding process. Different weld inspection techniques are applied on the welds and the details of weld defects analysis has been carried. Ultrasonic tests and Gamma and X-ray radiography methods are useful to find the internal weld joint defects. Liquid penetration and magnetic particle inspection techniques are suitable for surface and subsurface defects in weld samples. The kind of the weld defects and their nature in terms of the weld defect quantification and quality evaluation with each applicable NDT techniques is highlighted.

Keywords: Quality Control, NDT, Magnetic Field Leak, Acoustic Impedance.

Introduction

Mild steel is the most common steel material which occupies 85% of steel utility directly or for further processing. Quality assessment of this larger quantity is necessary. Most of the induction furnace units are engaged in production of mild steel ingots/billets and long products for mass consumption[1]. Carbon composition ranges from 0.34 to 0.44% unlike other grade steel which tend to be brittle yet malleable to make suitable for pipeline, structural compounds, construction material. It conducts electric current effectively without tarnishing the material surface in any way making it ideal for welding. Improper welding leads to innumerous flaws incorporated in welded and heat affected zone which needs to be identified and eliminated. According to quality assurance and standard requirements. To acquire this quality, various tests and methodologies are available and the best among those is non destructive evaluation. Non Destractive Evaluation is a wide group of analysis technique used in science and industry to evaluate the flaw in the material without causing damage to material, system or components. NDT does not permanently alter the article being inspected. It is highly valuable technique that can save both money and time in product evaluation, trouble shoot and research[2]. This paper reports various NDT methods which are discoursed on mild steel EN8 weld region for quality analysis and intensity of flaws in each technique.

Non destructive evaluation (NDE) techniques and their overview

Weld quality inspection of the structural components is very essential to maintain the long life and preventing failure while working under harsh environments like thermal/chemical and fatigue loads in various applications such pressure vessels or chemical plants. The non destructive examination procedures as per the prescribed codes are done on welded structures to realize the weld quality evaluation for the final acceptance. Various NDT techniques are used in the industry for defect detection applications. The major techniques for weld quality inspection are Visual Inspection, Liquid Penetrant Examination, Magnetic Particle Testing, X-ray radiography and Ultrasonic Inspection tests where the details can be found in different published references. The present work deals with the experiments carried on weld quality inspection procedure on samples of EN-08 steel specimens with different NDE techniques and the weld defects analysis.

Visual Inspection deals with the surface inspection for

any apparent visual defects, cracks, discontinuities, bead imperfections etc. on the weld surfaces and interface area with base materials. This provides the primary sight of the quality check on the physical surface condition of the sample and the weld quality. This is simple and primary inspection for the initial quality evaluation.

Liquid penetration process is relatively simple, low capital cost, the arrangement of discontinuities is not a limitation but it has its own limitations as it can inspect depth up to 2 mm. The defects need to open to surface and the testing procedure offers low reliability and moderate sensitivity requiring considerably high degree of operator skill. Test objects are coated with visible or fluorescent dye solution. Excess dye is removed from the surface, and a developer is applied. The developer acts as blotter drawing trapped penetrant out of imperfections open to surface. With visible dyes, vivid color contrasts between the penetrant and developer makes "bleed out" easily visible. With fluorescent dyes, ultraviolet light is used to make the bleed out fluorescence bright alloy imperfections readily seen. The principle of penetration testing is capillary action.

The principle of magnetic particle testing is flux leakage. It may be applied to raw material, billets, finished semi finished materials, welds and in-services parts. Magnetic particle inspection is not applicable for non-ferrous and austenite stainless steel. As the specimen is mild steel it can undergo magnetic particle inspection which is accomplished by inducing a magnetic field in a ferromagnetic material and then dusting the surface with iron particle (either dry or suspended liquid).Surface and near-surface imperfections distort the magnetic field and concentrated iron particle near imperfections, previewing a visual indication of the flaw[3].

Acoustic impedance mismatch is the working principle of ultrasonic inspection. The Ultrasonic probe transmits high-frequency sound waves ranges from 500 kHz to 10 MHz into the material to detect imperfections to locate changes in the material properties[4]. The most commonly used ultrasonic testing technique is pulse echo, where sound is introduced into a test object and reflections (echoes) are received from internal imperfection or form a part of geometrical surface, it is necessary that the discontinuity/flaw must be larger than one-half of the wavelength.

Passing highly penetrating electromagnetic radiation through an object and recording its image one film will develop[5] a radiography film to study. Differential absorption is the principle of radiography and the absorption is a function of density and thickness of the material.

A correlation is made with NDT methods like Liquid Penetration, Magnetic Particle, Ultrasonic, Radiography Inspection by knowing the weld defect signatures. According to ASTM standards and codes, this correlation saves time in real operation condition for establishing quality control[5].

Various Geometries

Materials and method

Mild steel is widely used in the applications like automobile, chemical plants, auxiliary components and manufacturing purposes. EN-8 is usually supplied in various forms like normalized or heat treated, quenched and tempered which is adequate for a wide range of applications. This is also very popular grade through medium hardening carbon steel which is readily machinable in any condition hence is considered as most suitable for the manufacture of various parts such as general-purpose axles and shafts, gears, bolts and studs. It can be further hardened typically producing components with enhanced wear resistance. It is also available in a free-machining version. EN8M in its heat treated forms possess good homogenous metallurgical

Table 1 – Applicable of NDT techniques for various defects and their performance.

Defect Type	V.I	P.T	M.P.T	U.T	R.T	A.E
Micro-crack	P	E	G	G	P	E
Macro-crack	E	E	E	E	O*	E
Porosity	G	G	E			
Surface Imperfections	G	E	E	G	P	E
Internal Imperfections	×	×	G	E	E	E
Brazing/bonding Welding	G	G	G	E	E	E
Inclusion	×	×	P	E	E	E

P= Poor; G= Good; E=Excellent; O* = Orientation dependent; ×= Not Applicable.

structures giving consistent machining properties.

Weld sample is fabricated with suitable dimension along with introducing cluster porosity, inclusion in weld region during tungsten inert gas welding to join the materials deliberately. After welding the length of the plates are 150 mm and 300 mm.

Procedure followed to make defective samples during TIG welding

Plate material	-	Mild steel EN-08
Plate Thickness	-	10 mm
Plate Width (Before weld)	-	75 mm
Plate length	-	300 mm
Main weld method	-	TIG welding (welding current 110 to 130 amperes).

As the test piece conditions is a mild steel (EN-08), TIG welded, type III penetrant that is both fluorescent and visible sensitivity level IV, water washable and non aqueous type 1 fluorescent developer have been chosen.

NDT techniques

Visual Inspection

The samples are examined for the weld quality evaluation for the EN-8 samples thoroughly for weld discontinuities and surface quality. No apparent defect is observed on the weld samples.

LP Testing

One of the straight forward inspection technique is Liquid Penetrant Inspection Technique, and the details of which are given below with steps followed.

Sensitivity comparison of liquid penetration test:

Calibration of Liquid Penetration test for sensitivity is carried out by comparison of water based at right MR 67 and glycols based MR 68 NF left. It found that water based penetrant showed high sensitivity due its low contract angle, viscosity and surface tension.

Pre cleaning (surface preparation)

The sensitivity of any penetrant examination procedure is greatly dependent upon the surrounding surface and discontinuity being free of any contaminant that might interfere with the penetrant process. The surface must be free from oil, grease, water, rust, scale, acids, even water or other contaminants that may prevent penetrant from entering flaw. The cleaning solvent used is volatile which does not leave any moisture.

Fig. 1 AL Comparative block

Penetrant application and dwell time

The water based duel (type -III) penetrant (MR 67) is applied effectively by brushing as shown in Fig 2 within the specified temperature range (*i.e.* 10 and 38°C). The penetrant is left on the surface for a sufficient time to allow as much penetrant as possible to be drawn from or to seep into a defect. Penetrant dwell time is the total time that a penetrant is in contact with the surface part. The time varies depending on the application penetrant material, the specific materials used, the nature of the part under examination (that is, size, shape, surface condition, alloy), and type of discontinuities expected[6]. Material density of mild steel is high and as penetrant is water based it shows excellent penetration properties *i.e.*, low contact angle and viscosity[7], 05 minutes dwell time is sufficient for good sensitivity inspection.

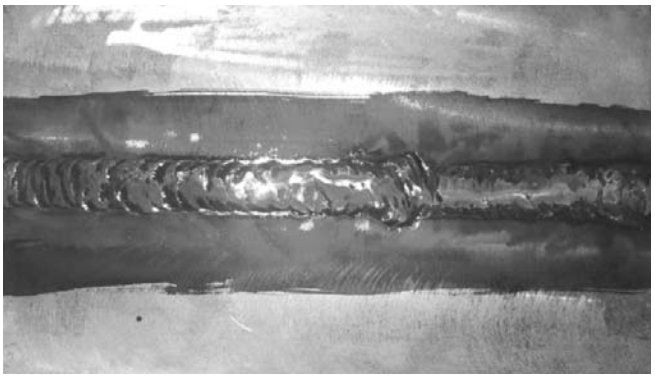

Fig. 2 After Penetrant Application

Process inspection

Inspection is performed under adequate white light (*i.e.* less than 2 ft candles (20 Lx)) to detect indication from any flaw which may be present[8]. As it is duel penetrant

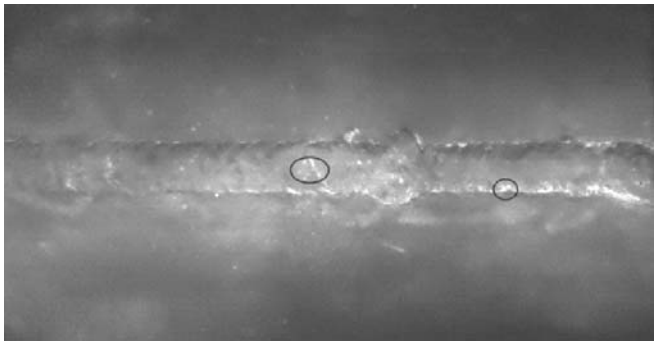

Fig. 3 Cluster Porosity Observed on the Specimen.

it was viewed under black light (U.V. light) and observed considerable sensitive cluster porosity at two places in the specimen as shown in Fig. 3.

Post cleaning of surface

Simple water rinse is processed thoroughly to clean the parts of surface, to remove the residual penetrant or developer from the parts that were found to be acceptable.

Magnetic particle inspection :

Magnetic particle inspection is one of the potential techniques to inspect the subsurface defects like cracks, laps, seams micro-cracks and discontinuities on or near surface material. The procedure applied in this technique is shown below in detail[9]. White back ground film is applied over the inspection for better inspection practice.

Calibration of magnetic partial equipment (Yoke):

To attain best sensitivity of flaw, yoke need to be calibrated according to ASTM standard that is it needs to lift a weight of 10 lb in Alternative Current (AC) and 40-50 lb in Direct Current (DC) that indicates the magnetic field strength and depth of penetration in Figure 5. It is also examined under ASTM test block and absorbed six lines clearly shown in Fig. 4.

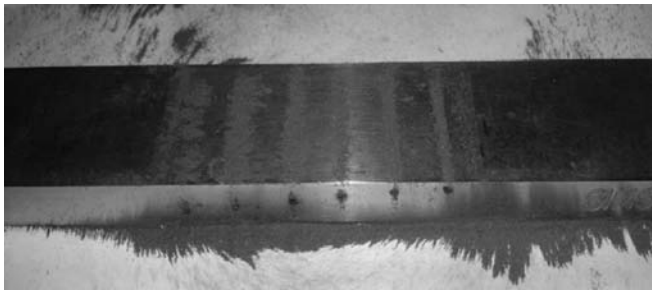

Fig. 4 ASTM test block.

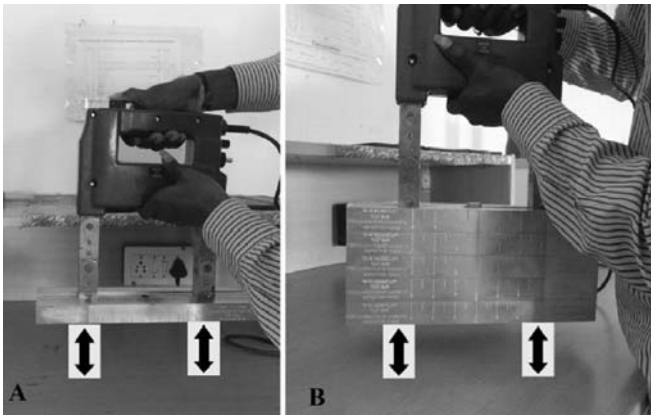

Fig. 5 Calibration of yoke in AC (A) and DC (B) mode

Introducing magnetic field :

Longitudinal Magnetic field is induced in the specimen with the help of indirect magnetic field Yoke. Direct current is preferred for deep possible penetration. These longitudinal magnetic lines will pass through the material and if any gap or interruption occurred, the magnetic flux leak will take place in that area. At this point, magnetic flux is highly comparative to other areas.

Magnetic particle application :

Dry magnetic particles are dispersed over the white backgrounder inspection area. It is due to the magnetic flux leak, the magnetic particles accumulate over the defects.

Inspection procedure :

Examined under sufficient light intensity of 100 ft (1000 Lx)[10], defects are viewed clearly and cluster porosity is observed on the specimen at different places as shown in Fig. 6.

Ultrasonic investigation

Ultrasonic technique is the potential for probing the weld defects through the weld joint. As the inspection

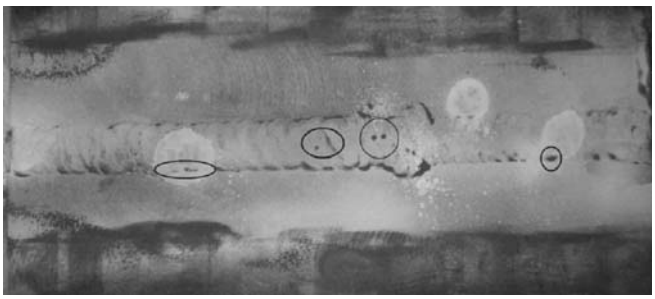

Fig. 6 Custer porosity absorbed at different position

area is weld region we cannot directly place probe over weld region. The procedure adapted is pulse echo technique with angle probe of 45°, shear wave development for inspection.

Calibration of the ultrasonic flaw detector (Make: Modsonic; Model: Da-Vinci-alpha) is done according to ASTM standards by using V2 blocks for angle probe sensitivity. Adjustments are carried out using zero key, range, material velocity angle. Measurements which are set to 'on' and other parameters and given to device for inspection conditions sensitivity are level of ultrasonic flaw detector with angle beam probe 45°, X off is found to be 10 mm as shown in Fig. 7 and given feed to equipment by considered tolerances as + 1 or –1 on Sound path[11].

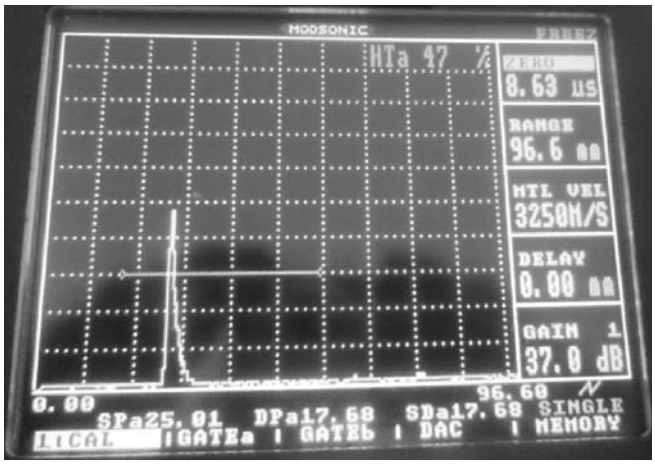

Fig. 7 Calibration of V2 Block

Generating distance amplitude curve :

The use of electronic methods to compensate for attenuation losses as a function of ultrasonic metal travel distance may be employed by DAC curve[12]. Specimen reference DAC block is prepared with same grade material of that need to be inspected having dimensions 40 mm thickness and hole drilled subsequently at ¼ t = 10, ½ t = 20, ¾ t = 30 on the DAC block. By considering the thickness of the DAC block sound path, surface distance is calculated. Actual sound path and surface distance are extracted from the device by amplitude response from the DAC block. Capture the amplitude of first hole by placing the probe at a surface distance of 10 mm and sound path 14. 14. Adjust the instrument gain to attain 80% echo, enter this reading in DAC menu by using enter key as first point, similarly carry this procedure without changing the sensitivity control, obtain maximum amplitudes from second and third hole without altering gain[13]. Due to sound attenuation and hole diameter difference in the actual values from calculated values, amplitude of first each is 80% and second echo is less than the 1st *i.e.,* 34% and the third echo is less than 2nd *i.e.,* 26% as plotted in Table 2. Feed the peaks of the indications of echo on the screen by entering 2 and 3 points in DAC menu. Connect the screen marks by pressing DAC ON to provide the distance amplitude curve for the side-drilled hole as in Fig. 8. The line in DAC curve represent that if a echo crosses upper line it implies reject, second one for repair and bottom line for acceptance.

Inspection procedure :

Inspection is carried over the work piece by applying 2T oil as couplant over weld and HEZ (Heat Effect Zone).

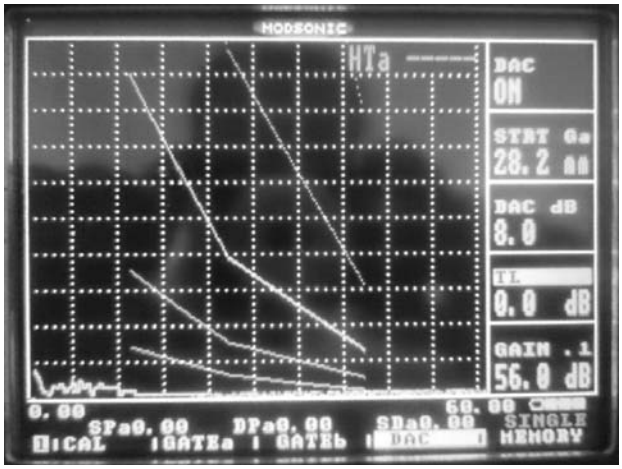

Fig. 8 DAC Curve

Table 2 – Table of data to draw DAC Curve

S.No	Thickness T=40	Actual surface distance	Actual Beam path	Ref Db
1	¼ t = 10	9.39	13.29	56.0
2	½ t = 20	19.07	26.98	54.9
3	¾ t = 30	31.07	43.95	63.3

All units are in mm.

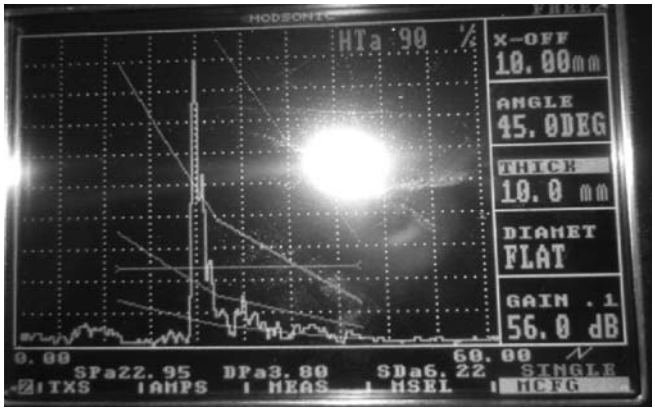

Fig. 9 Defect echo in A- scan

A scan in thoroughly carried over entire specimen and found sharp echo's at different places typically some crossed reject line are shown in Fig. 9 at a depth of 3.80 from surface and amplitude of echo 90% cutting off reject line.

Fig. 9 B scan image of Defect echo

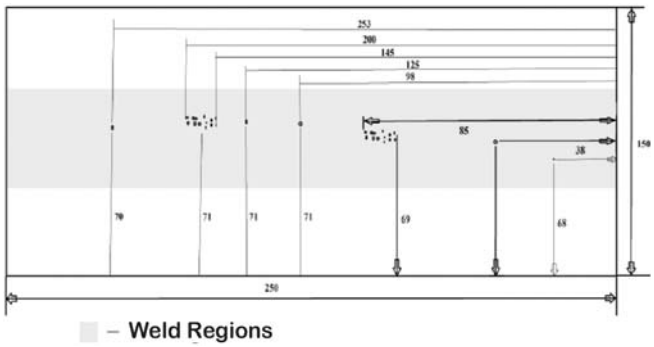

Fig. 10 Defectogram

Freerun B scan is also recorded in specific places where continuous higher sharp echo is found measured from

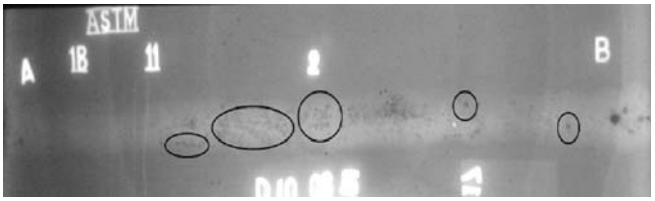

Fig. 11 Cluster Porosity and Inclusion

right 70 mm to 85 mm and 145 to 200 mm on the specimen which is vividly depicted in defectogram Fig. 11 . The echoes are above acceptance line of DAC Curve which are at a depth of 2.74 mm with an amplitude of flaw 67% (with the help of curve). Other pin holes and minor defects under repair line need to be repaired which are at 6 mm depth[14] and no defects are found in heat affected zone region.

This technique provides the weld quality defects evaluation through the reference defects which are calibrated prior with known defects. Hence this requires expertise in carrying out the inspection and interpretation of the results for the defects confirmation and it may be treated as cluster porosity.

X-Ray Radiography Testing

It involves exposing a test sample to penetrating radiation (with high energy) so that the radiation passes through the object being inspected and their recording medium is placed against the opposite side of that object[15]. The part is placed between the radiation source and a piece of film will stop some of the radiation. Thicker and denser areas will stop more radiation. The film darkness will vary with the amount of radiation that reaches the film through the test object. The minimum recommended thickness limitation may be reduced when the radiography techniques are used to demonstrate that the required radiography testing sensitivity has been obtained. Radiography test is conducted on the sample. Wire type and hole type pentameters are taken for test accuracy[16]. The sensitivity achieved is good and the defects in the film are observed easily. Cluster porosity is absorbed extensively in radio graphic film over weld region.

Results and Discussion

- Surface defects and discontinuities are detected through Liquid Penetration test illustrated in Fig. 3. Subsurface defects cannot be identified but are fixed flaws which are open to surface with high sensitivity of about 20 microns.

- Surface and sub-surface discontinuities are detected through magnetic particle inspection illustrated in Fig. 6. The cluster porosity is detected.
- Two internal discontinuities were detected through ultrasonic testing and are shown in Fig. 9, 10. It is due to near dead zone surface that the defects are hard to identify at surface as accurately as liquid penetration and magnetic particle test.
- Radiography film gives us a clean and solid copy of film to interpret the cluster porosity location, orientation and storage capacity of films.
- Over all the results that are attained from ultrasonic and radiography are highly sensitive than other two NDE techniques for weld quality inspection procedures. Still the inexpensive testing magnetic particle inspection also gave sufficient information about defects porosity and cluster porosity in present near surface and deep up to depth of 6 mm in the surface as per U.T. investigation.

Acknowledgements

Authors are grateful to AICTE (Project no: 8023/RID /RPS-58/ (Policy-111) [PVT]) for sanction of grant-in-aid to carry out the project work. We owe indebt gratitude and acknowledgements to "Dr H S Saini, Managing Director and Sardar G S Kohli, Vice Chairman, Guru Nanak Institutions, Ibrahimpatnam for their cooperation and encouragement.

References

1 Ministry of Steel "Report of the working group on steel industry for the twelfth five year plan (2012 - 2017)"

2 **Georgeou G.A.**, "Non-Destructive Testing and Evaluation of Metals", Material Science and Engineering, 3.

3 **Lari E.** and **Rajeev Kumar E.** "Basics of Non-Destructive Testing", Ludhiyana (Panjab) (2013).

4 ***Jolly M.R. et al.***, "Review of Non-destructive Testing (NDT) Techniques and their applicability to thick walled composites" *Elsevier B.V, Science Direct Procedia CIRP* **38** (2015) 129-136.

5 American Society for Metal Hand book "Non Destructive Inspection and Quality Control" ASM Metals Park, Ohio. **11**.

6 American Society of Mechanical Engineers "Standard test method for liquid penetrant examination" SE-165 (Identical with ASTM Specification E 165-95)

7 **Larson B.** "Study of the Factors Affecting the Sensitivity of Liquid Penetrant Inspections: Review of Literature Published from 1970 to 1998" DOT/FAA/AR-01/95, AFS-300.

8 **Nielson D.C.** and **Thompson J.G.H.**, "Evaluation of Liquid Penetrant Systems, Materials Evaluation", **33**(12) (1975) 284-292.

9 "ASTM E-709-01 Standard Guide for Magnetic Particle Examination and ASTM E-1444-01 Standard Practice for Magnetic Particle Examination.

10 **Chedister William C.**, "Evaluation of Magnetic Gradients for Magnetic Particle Testing", Materials Evaluation, **60**(9) (2002) 1083-1089.

11 **Nanekar P.P.** and **Shah B.K.**, "Characterization of Material Properties by Ultrasonic's" *BARC News letter*, 249.

12 American Society of Mechanical Engineers "Standard practice for ultrasonic Examination of longitudinal welded Pipe and tubing" Identical with ASTM Specification E 273-83.

13 American Society of Mechanical Engineers "Standard Practice for Ultrasonic Contact Examination of Weldments" This standard is issued under the fixed designation E 164.

14 **Ranganayakulu S.V., Kucheludu1 A., Gowtham1 R.** and **Ramesh Kumar B.**, "Inspection on aluminum plates by implementation of NDT techniques" *J. Pure Appl. Ultrson.* **37** (2015) 57-61.

15 ASTM E 592 Guide to Obtainable ASTM Equivalent Pentameter Sensitivity for Radiography Of Plates ¼ to 2 in .thick with X rays and 1 to 6 in thick with Cobalt-60.

16 NDT Evaluation method of aerospace and nuclear materials "National Symposium on ultrasonic" (ISBN) No. 24-25 January, Ravens haw University, Cuttack (2014) 12-1-6.

J. Pure Appl. Ultrason. 38 (2016) pp. 65-70

Synthesis and study of thermo acoustic properties of α-Al_2O_3 nano suspension in ethanol base fluid

N.R. Pawar[1*], O.P. Chimankar[2], S.J. Dhoble[2] and G.A. Aghalte[3]

[1]Department of Physics, Arts, Commerce and Science College, Maregaon-445303, India
[2]Department of Physics, RTM Nagpur University, Nagpur-440033, India
[3]Department of Physics, Lokmanya Tilak Mahavidyalaya, Wani-445304, India
*E-mail: pawarsir1@gmail.com

The present paper reports the synthesis and study of thermo acoustic properties of alpha alumina (α-Al_2O_3) nano suspension in ethanol base fluid. α-Al_2O_3 nanoparticles were synthesized through alkoxide route using sol-gel method. Aluminum isopropoxide Al $(OC_3H_7)_3$, and aluminum nitrate nanohydrate Al $(NO_3)_3$ 9 H_2O were used for preparing alumina solution. Sodium dodecylbenzene sulfonate (SDBS) was used as the surfactant stabilizing agent. The sample was characterized by X- ray diffraction (XRD) and scanning electron microscopy (SEM). Average particle size has been estimated by using Debye-Scherrer formula. The ultrasonic velocity measurement at 4 MHz with an interferometric technique has been made on alpha alumina (α-Al_2O_3) nano suspension in ethanol base fluid. Measurements were also taken for the density and viscosity. The thermo acoustic parameters were calculated from the velocity, density and the viscosity measurements. By taking measurements over entire range of concentrations and temperatures, we obtained information about the aggregation of nanoparticles in the suspended medium. Thermo acoustic parameters are related to the surface of nanoparticles and nanoparticle surfactant interactions and help for the study of thermo acoustic properties of nanosuspension.

Keywords: α-Al_2O_3; ethanol; XRD; SEM; Thermo acoustic parameters.

Introduction

The ultrasonic sound velocity and the thermodynamic parameters derived from it have been widely used to interpret the interactions between nanosuspensions in the base fluid. There has been an increasing interest in the study of interactions between the nanoparticles in the suspended medium[1-2]. Ultrasonic study of nano-suspension has been extensively carried out in different branches of science to measure the thermodynamic properties to predict the nature of interactions of nanosuspension in base fluid[3-4]. Ultrasonic velocity and thermo acoustic parameters as a function of the concentration in nanoparticle suspension are useful in gaining insight into the structure and bonding of associated nano complexes and other processes in nanosuspension. The materials of interest in this study are α-Al_2O_3 and ethyl alcohol (C_2H_5OH). Thus ethyl alcohol has an OH group that might be expected to lead to the formation of a hydrogen-bonded nano complex with α-Al_2O_3 at the oxygen site and perhaps electrostatic bonding at the other sites. These types of nanosuspension are of interest to organic chemists who want to know about the type of bond and the number of each kind of nanoparticles in the α-Al_2O_3 nano complex.

In this work, measurements of the velocity, adiabatic compressibility, relaxation time, internal pressure, acoustic impedance and other related thermo acoustic parameters as functions of concentration and temperatures are reported. The data presented may stimulate other researchers to consider the interactions of nanoparticles in nanosuspension. Such data are valuable in building a core of basic information about nanosuspension. The method used in the measurement of ultrasonic velocity at 4 MHz was the interferometric method over the temperature range 25-40°C.

α-Al_2O_3 is one of the most widely used oxide ceramic material. It is used in a variety of plastics, rubber, ceramics, and refractory products. As the α-phase

ultrafine Al_2O_3 is a high performance material of far infrared emission, it is used in fiber fabric products and high pressure sodium lamp as far-infrared emission and thermal insulation materials. In addition, α-Al_2O_3 with high resistivity and good insulation property, it is widely used as the main components for YGA laser crystal and integrated circuit substrates. Therefore α-Al_2O_3 nanoparticle was select for proposed study. In the present investigation the synthesis of α-Al_2O_3 nanoparticles by sol-gel method is discussed. The main objective of present work is to contribute the nanosuspension properties database in current literature in order to better understand the effects of various parameters such as particle size and temperatures. Ultrasonic velocity and thermo acoustic parameters are highly dependent on specific surface area of nanoparticle in nanosuspension.

Experimental methods

The test liquid samples used were of spectroquality. All these samples are of BDH analar grade and were assume to be sufficiently pure so that no further purification was necessary. In this study the ultrasonic measurements have been made by interferometric method at fixed frequency 4 MHz over the entire range of concentrations and in the temperature range 25-40°C. The velocity of ultrasound thus measured was accurate to within 0.01%. The viscosity of the suspension was measured using a Brookfield rotating cylinder viscometer. The densities were measured with an Anton Paar DMA 35 N vibrating tube densimeter with a $\pm$ 0.5 × 10^{-3}g/cm^3 resolution. The temperature of nanosuspension medium was controlled to within 0.2°C.

Preparation of Samples

Nanoparticles of alpha alumina (α-Al_2O_3) was prepared by sol-gel method[5-9] from Aluminum isopropoxide [Al $(OC_3H_7)_3$] and aluminum nitrate. Starting solution was prepared by adding aluminum isopropoxide [Al $(OC_3H_7)_3$] gradually in 0.2 M aluminum nitrate and solution continuously stirred for 48 hours. Later, Sodium dodecylbenzen sulfonate (SDBS) was added and stirred for one hour. Now this solution were heated up to 60°C and stirred constantly for evaporation process. Now the paste so obtained was heated at 90°C for 8 hours, we get nanoparticles of alpha alumina (α-Al_2O_3) in powder form.

The prepared sample were characterized for their phase purity and crystallinity by X-ray powder diffraction (XRD) using PAN-analytical diffractometer (Cu-Ka radiation) at a scanning step of 0.01°, continue time 20 s, in the 2h range from 10° to 120°. Formation of the compound confirmed by XRD pattern matched with the standard data available in JCPDS file. From this study, average particle size α-Al_2O_3 has been estimated by using Debye-Scherrer formula

$$D = \frac{0.9\lambda}{WCos\theta} \quad (1)$$

Where 'λ' is the wavelength of X-ray (0.154060nm), 'W' is FWHM (full width at half maximum), 'θ' is the diffraction angle and 'D' is particle diameter (size). The average estimate size of α-Al_2O_3 nano particles is found to be 20-30 nm. The prepared α-Al_2O_3 nano particles were suspended in ethanol. Fig.1 represents XRD pattern of α-Al_2O_3 nanoparticles and Fig. 2(A) and 2(B) represents SEM images of α-Al_2O_3 nanoparticles.

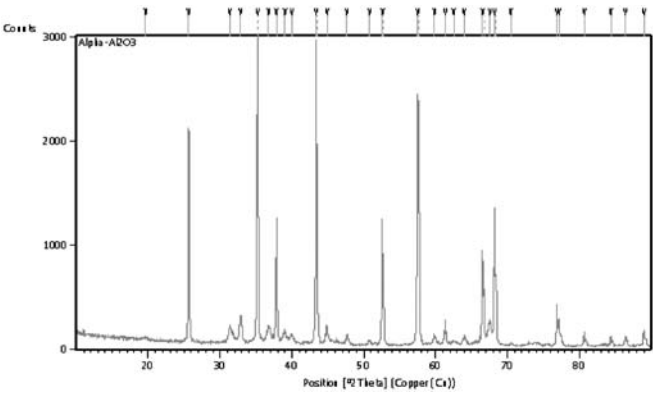

Fig. 1 XRD pattern of α-Al_2O_3 nanoparticles.

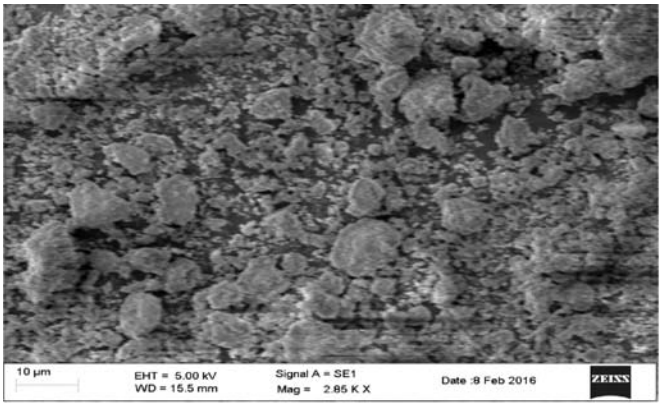

Fig. 2(A) SEM image of α-Al_2O_3 nanoparticles

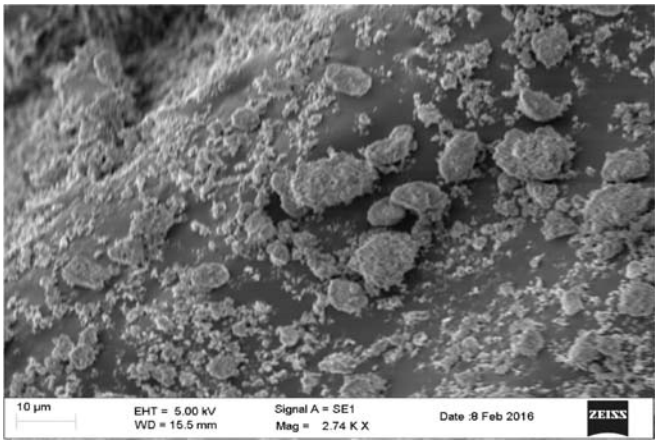

Fig. 2(B) SEM image of α-Al_2O_3 nanoparticles.

Results and Discussion

The results of measurement at 25-40°C for α-Al_2O_3 nanosuspension in ethanol base fluid are shown in Fig. 3, where the ultrasonic velocity are plotted versus molar concentration. The ultrasonic velocity propagation shows analogous behavior with molar concentration of α-Al_2O_3 nanoparticles in ethanol. The non linear variation of ultrasonic velocity versus molar concentration helps for the study of structure and bonding of associated nano complexes[10-13]. The ultrasonic velocity exhibited maximum value at 25°C and decreases with temperature because of thermo-elastic losses which arises due to the Brownian motion of nanoparticles in suspended medium. There is formation of hydrogen bond due to hydrogen atom of ethanol (C_2H_5OH) attached to a strongly electronegative oxygen nanoparticle of α-Al_2O_3. Looking into the behavior of nanoparticles, it can be understood that, the broad maxima in the velocity curve at 0.06 are attributed to the molecular associations, complex formations due to hydrogen bond; where as minima at 0.04 and 0.08 indicates dissociations of nanoparticles in nanosuspension. The measurement of sound velocity of α-Al_2O_3 nanosuspension in ethanol base fluid is important as a reference study in relative, automatic ultrasonic velocity measurements, which is often required in an industrial process line.

For further analysis and interpretation, adiabatic compressibility, relaxation time, acoustic impedance, internal pressure, free volume, free length, molar sound velocity, molar compressibility and Vander Wall's constant were calculated using our measured values of ultrasonic velocity, density and viscosity.

The Adiabatic compressibility versus molar concentration at 25-40°C for α-Al_2O_3 nanosuspension in ethanol base fluid are shown in Fig. 4. The adiabatic compressibility of nanosuspension is a thermodynamic parameter of fundamental significance. It enables direct access to the nanosuspension structure in terms of the particle packing density and the inter particle forces. The adiabatic compressibility shows the reverse trend as that of ultrasonic velocity which is theoretically accepted. The non-linear variation of adiabatic compressibility with molar concentration indicates the presence of phase separation in nano suspension. Adiabatic compressibility of α-Al_2O_3 nanosuspension show minima at molar concentration 0.06, indicating nanoparticles are more rigid in this concentration region. This may mean that a more stable nano complex is formed with electronic bonds of two different strengths, one hydrogen bond and other a weaker electrostatic bond.

Acoustic impedance is found to be almost reciprocal of adiabatic compressibility. The Acoustic impedance versus molar concentration at 25-40°C for α-Al_2O_3 nanosuspension in ethanol base fluid are shown in Fig. 5.

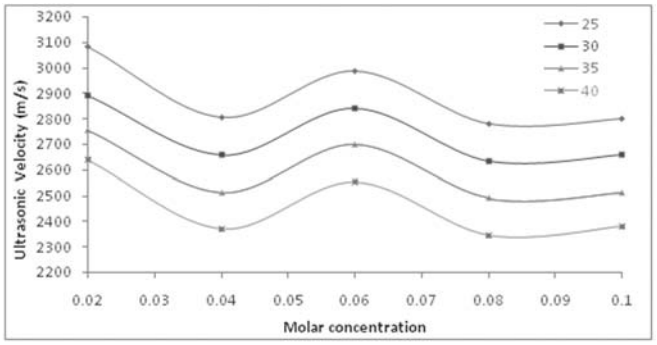

Fig. 3 Ultrasonic velocities versus molar concentration of α-Al_2O_3 nanosuspension in ethanol.

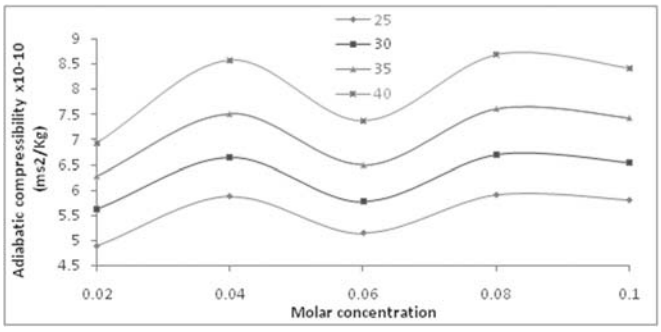

Fig. 4 Adiabatic compressibility versus molar concentration of α-Al_2O_3 nano suspension in ethanol.

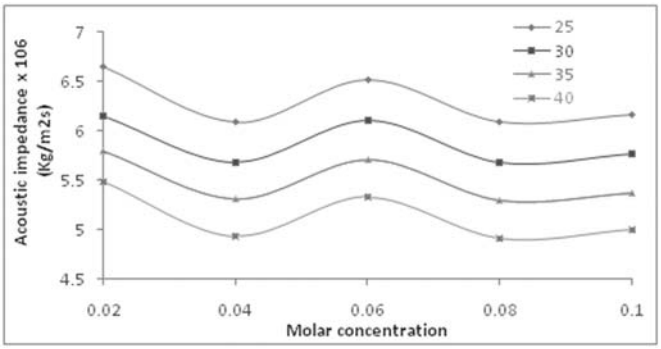

Fig. 5 Acoustic impedance versus molar concentration of α-Al_2O_3 nanosuspension in ethanol.

Acoustic impedance show similar trend as that of ultrasonic velocity, it is in good agreement with the theoretical requirement. Peak at 0.06 is due to the aggregation of nanosuspension in ethanol base fluid.

The relaxation time versus molar concentration at 25-40°C for α-Al_2O_3 nanosuspension in ethanol base fluid are shown in Fig. 6. It is depends on viscosity and adiabatic compressibility. It shows similar behavior as that of adiabatic compressibility. It is caused by the energy transfer between translational and vibrational degrees of freedom. Minima at molar concentration 0.06, indicating nanoparticles are more rigid in this concentration region.

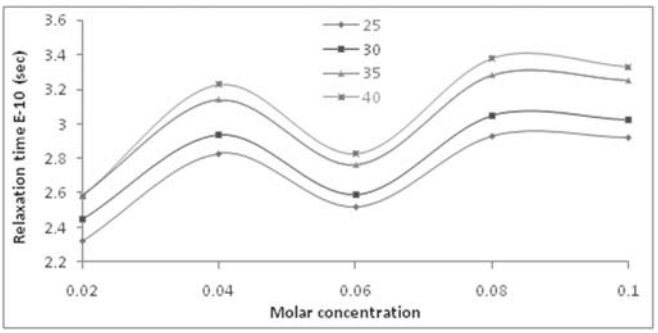

Fig. 6 Relaxation time versus molar concentration of α-Al_2O_3 nanosuspension in ethanol.

The concentration dependence of the internal pressure and free volume of α-Al_2O_3 nanosuspension in ethanol are shown in Fig. 7 and Fig. 8. Internal pressure and free volume shows reverse trend which is in good agreement with the theoretical requirement. In this case internal pressure and free volume curves indicates association through hydrogen bonding at molar concentration 0.06. This suggests close packing of the molecules inside the

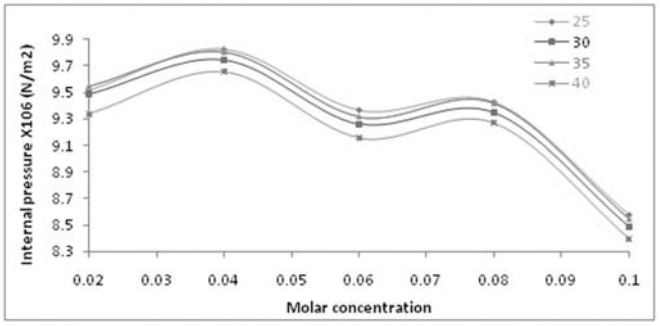

Fig. 7 Internal pressure versus molar concentration of α-Al_2O_3 nanosuspension in ethanol.

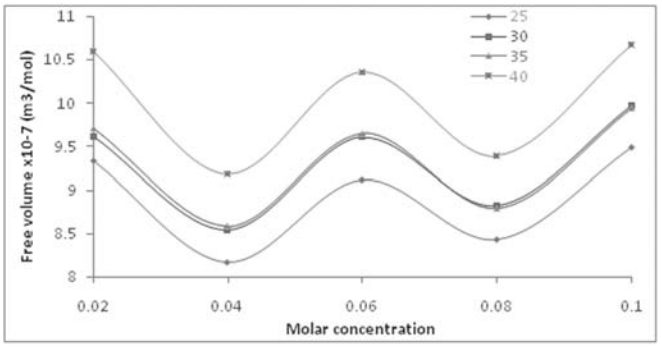

Fig. 8 Free volume versus molar concentration of α-Al_2O_3 nanosuspension in ethanol.

shield in this region. Internal pressure and free volume of nanosuspension are highly useful in understanding nature of interactions, internal structure and the aggregation behavior.

The intermolecular forces, which in one way or another determine the said properties of nanosuspension, consist of attractive forces and repulsive forces. These forces have opposite directions but are numerically equal under given external conditions. The attractive forces are dependent on the distance between what are called the centres of attraction of the nanoparticles, whereas the repulsive forces are dependent on the distance between the surfaces of the nanoparticles. Centres of attraction do not coincide with the geometrical centre of the nanoparticles. The distances between the surfaces have a clear physical significance, and thus lend themselves more easily. Surface tension, viscosity, thermal expansion and molecular association will be related to the intermolecular free length. Free length is long, ultrasonic velocity has a low value. Its value corresponded to the molecular shape Fig. 9 contains the plot of free length versus molar concentration. It shows similar trend as that

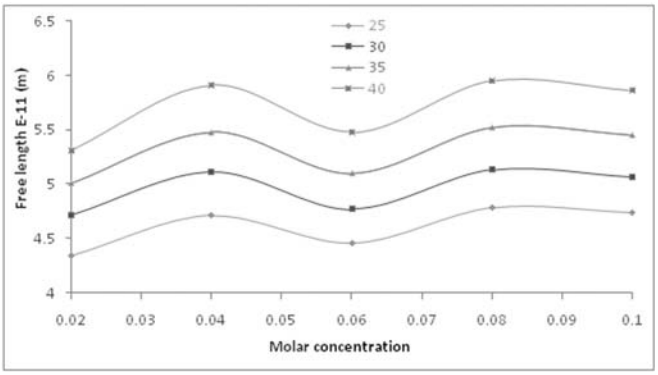

Fig. 9 Free length versus molar concentration of α-Al_2O_3 nanosuspension in ethanol.

of adiabatic compressibility and reverse trend as that of ultrasonic velocity which is in good agreement with the theoretical requirement.

Fig. 10 and Fig. 11 contain the plots of molar sound velocity and molar compressibility versus molar concentration of α-Al_2O_3 nanosuspension in ethanol. Increase in the values of these parameters predicts strong interactions in the interacting nanosuspension. These parameters help for the study of range of repulsive and attractive forces between nanoparticles in nano-suspension. These thermo acoustic parameters show similar trend as that of ultrasonic velocity.

The Vander Waal's constant versus molar concentration at 25-40°C for α-Al_2O_3 nanosuspension in ethanol base fluid are shown in Fig. 12. It shows similat trend as that of ultrasonic sound velocity, it is in good aggreement with theoretical requirement. The maxima at 0.06 shows association of nanoparticles due to closed packing of the interacting nanosuspension inside the shell. The change in van der Waal's constant would be due to a change in intermolecular geometry.

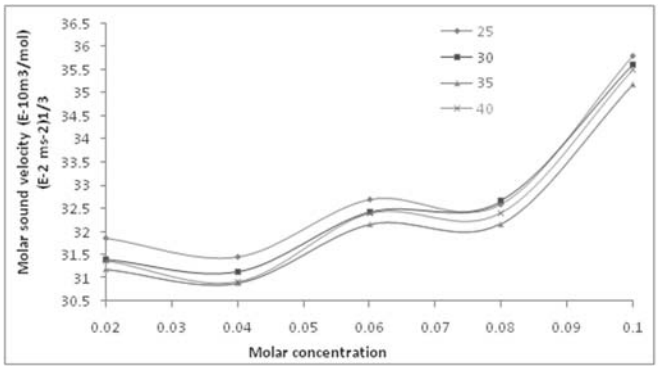

Fig. 10 Molar sound velocity versus molar concentration of α-Al_2O_3 nanosuspension in ethanol.

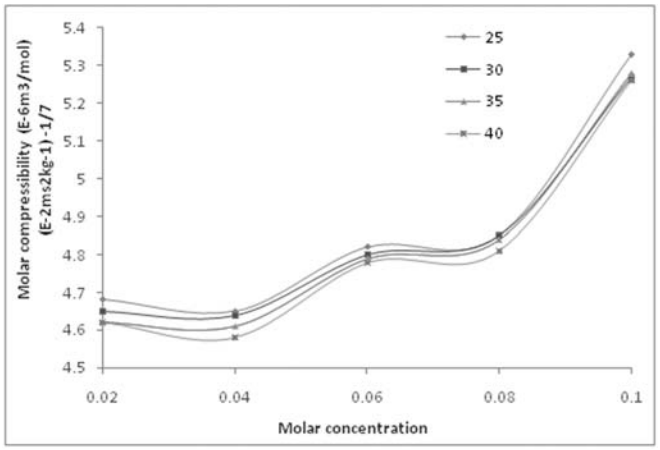

Fig. 11 Molar compressibility versus molar concentration of α-Al_2O_3 nanosuspension in ethanol.

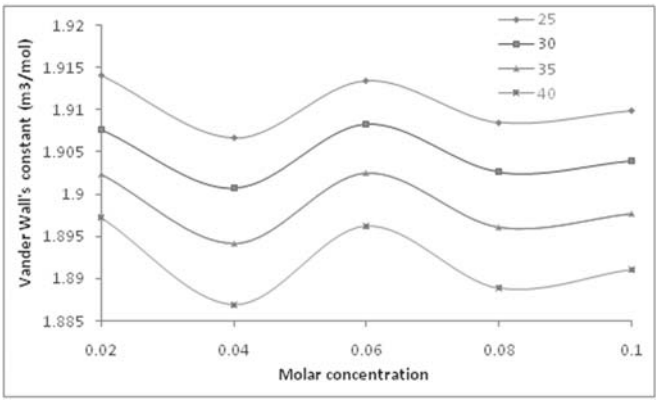

Fig. 12 Vander Wall's constant versus molar concentration of α-Al_2O_3 nanosuspension in ethanol.

Conclusion

- The ultrasonic velocity and thermo acoustic parameters show considerable deviation from any linear variation with respect to molar concentrations.
- Non linear variation of ultrasonic sound velocity and thermo acoustic parameters versus molar concentration are due to Brownian motion of nanoparticles in nanosuspension.
- Behavior of nanoparticles in ethanol base fluid nano suspension dependent on its specific surface area.
- Thermo acoustic parameters are highly useful in understanding nature of interactions, internal structure and the aggregation behavior.

References

1. **Kumar D.H., Patel H.E., Kumar V.R.R., Sundararajan T., Pradeep T.** and **Das S.K.,** Model for heat conduction of nanofluids, *Phy. Rev. Let.,* **94**(14), (2004) 1-3.
2. **Rajagopalan S., Sharma S.J.** and **Nanotkar V.Y.**, Ultrasonic Characterization of Silver Nanoparticles, *J. Metast. and Nanocryst. Mat.,* **23**, (2005) 271-274.
3. **Gan Z., Ning G., Lin Y.** and **Cong Y.,** Morphological control of mesoporous alumina nanostructures via template-free solvothermal synthesis. *Mater. Lett.*, **61**(31), (2007) 3758-3761.
4. **Zhan X., Honkanen M.** and **Leva E.**, Transition alumina nanoparticles and nanorods from boehmite nanoflakes. *J. Crystal. Growth,* **310**(30), (2008) 3674-3679.
5. **Park Y.K., Tadd E.H., Zubris M.** and **Tannenbaum R.**, Size controlled synthesis of alumina nanoparticles from aluminum alkoxides, *Mat. Res. Bull.*, **40**(9), (2005) 1512.
6. **Wang D.G., Guo F., Chen J.F., Liu H.** and **Zhag Z.**, Preparation of nano aluminium trihydroxide by high gravity reactive precipitation, *Chem. Eng. J.*, **121**(2-3), (2006) 109-114.
7. **Aghababazadeh R., Mirhabibi A.R., Pourasad J., Brown A., Brydson A.** and **Ameri Mahabad N.**, Economical synthesis of Nanocrystalline alumina using an environmentally low-cost binder, *J. Surf. Sci.*, **601**(13), (2007) 2864-2867.
8. **Christian P.** and **Bromfield M.**, Preparation of small silver, gold and copper nanoparticles which disperse in both polar and non-polar solvents, *J. Mater. Chem*, **20**, (2010) 1135-1139.
9. **Rogojan R., Andronescu E., Ghitulica C.** and **Stefan B.**, Synthesis and characterization of alumina nano-powder by sol-gel method. *UPB Sci. Bull. Ser. B*, **73**(2, 27), (2011) 67-76.
10. **Bhalla V., Kumar R., Tripathi S.** and **Singh D.**, Mechanical and thermal properties of praseodymium nanoparticles: an ultrasonic study, *Int. J. Mod. Phys. B,* **27**, (2013) 1350116.
11. **Pawar N.R.**, Ph.D thesis Summary on Investigation of Ultrasonic wave absorption in some Bio-liquids, *J. Pure Appl. Ultrasonic.*, **36**, (2014) 69.
12. **Pawar N.R.** and **Chimankar O.P.**, Comparative Study ultrasonic absorption and relaxation behavior of polar solute and non-polar solvent, *J. Pure Appl. Ultrasonic.*, **37**, (2015) 11.
13. **Singh D.** and **Pandey D. K.**, Ultrasonic investigations in intermetallics, *Pramana*, **72** (2009) 389-398.

J. Pure Appl. Ultrason. 38 (2016) pp. 71-75

Comparison between capacitive micromachined ultrasonic transducers with circular and square microplates

Rashmi Vashisth, Satvika Anand* and Srishti Bhickta

Department of Electronics and Communication Engineering,
Amity School of Engineering and Technology, Bijwasan, New Delhi-110061, India
*E-mail: satvikaanand25@gmail.com

The Capacitive Micromachined Ultrasonic Transducers (CMUTs) are constructed on silicon substrate in which one electrode is highly doped at top and other is metal layer on suspended silicon membrane resting on silicon dioxide walls. The moving part of CMUT wall is made from silicon nitride membrane. They are efficient transmitters and receivers for air coupled non-destructive evaluation applications, generating or detecting ultrasonic waves by vibrating membrane featuring fixed circumference. Despite the advantages and their broad bandwidth, studies indicates that the overall sensitivity of CMUT's need to be improved to match piezoelectric transducers. This paper presents an approximate analytical solutions and comparison between circular and square plates for the static deflection caused by electrostatic forces and pull-in voltage by using MATLAB. The evaluation of the electrostatic force between the two plates is simplified due to the fact that the electrostatic gap is much smaller than lateral dimensions of the device. This has been seen that the deflection of circular is better than the square microplates. These theoretical analyses are helpful for design and optimization of such devices.

Keywords: Ultrasonic transducer, Electrostatics, Static deflection, Electrostatic force, Pull-in voltage.

Introduction

The Capacitive micromachined ultrasonic transducers (CMUT's) have become the choice of technology for a wide range of applications such as medical diagnostic imaging, non-destructive testing, material characterization, and automotive collision avoidance applications like park assist or blind spot monitoring. This type of sensors exhibit many advantages over their piezoelectric counterparts, such as inherently low power consumption, very high resolution and sensitivity, excellent stability and durability, lower sensitivity to temperature variations, low noise features[1]. The typical CMUT geometry is built with a square, circular diaphragm separated from a fixed back plate by a small air gap. CMUTs are the transducers where the energy transduction is due to change in capacitance.

The physical and chemical properties of liquid mixture can be studied by the non-linear variation of ultrasonic velocity, Lennard Jones potential repulsive term exponent, relative association and interaction parameter with concentration in a liquid mixture.

CMUT

A CMUT is simply a device with two plate-like electrodes biased with a DC voltage and driven with an additional AC signal to harmonically move one of the plates. The main components are the cavity, the membrane, and the electrode.

Materials Used

The device is constructed on silicon substrate in which one electrode is highly doped at top and other is metal layer on suspended silicon membrane resting on silicon dioxide walls. The moving part of CMUT wall is made from Silicon membrane.

Various Geometries

The various geometries present for CMUT plates are circular, square and Hexagonal. In this paper, we present a distributed parameter model to determine the deflection of the circular and square plate subjected to non-uniform electrostatic forces.

Formulation and Simulation for Circular shaped membrane in CMUT

The model is based on the Kirchhoff-Love assumptions that the plate is thin and the deflections and slopes are small[2]. A schematic of the device structure is shown in Fig.1. The material and other geometrical parameters are summarized in Table 1.

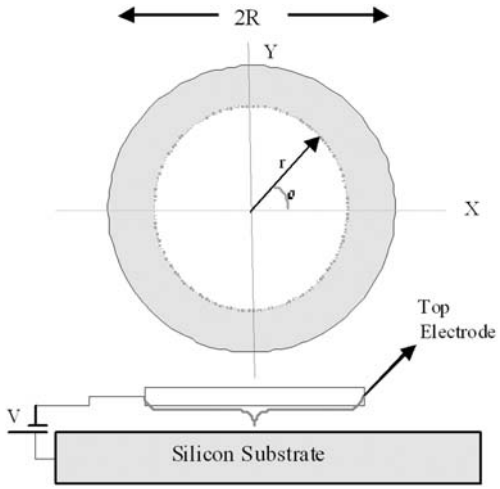

Fig 1. Clamped Circular CMUT

Table 1 – Parameters used in simulation

Material	Silicon
Radius, R	45 μm
Thickness, t	1 μm
Young's Modulus, E	130 GPa
Poisson's ratio, v	0.23
Density, ρ	2330 kg/m^3
Initial gap, d_0	1 μm
Dielectric constant, ε_o	8.85×10^{-12} F/m

The model is based on the Kirchhoff-Love assumptions that the plate is thin and the deflections and slopes are small.

Governing equation for deflection of a thin elastic circular plate of radius R and thickness t is given by Eq. (1), where $0 \le r \le R$, $w(r)$ is the Displacement of plate at any radial position, r and $Q(r)$ is the Electrostatic force per unit area on the top plate.

$$\frac{d^4w}{dr^4}+\frac{2}{r}\frac{d^3w}{dr^3}-\frac{1}{r^2}\frac{d^2w}{dr^2}+\frac{1}{r^3}\frac{dw}{dr}=\frac{Q(r)}{D}$$

$$\textit{Flexural Rigidity, } D=\frac{Et^3}{12\left(1-v^2\right)}$$

The electrostatic force per unit area acting on the upper plate is given by,

$$Q(r)=\frac{\epsilon_0 V^2}{2\left(d_0-w(r)\right)^2} \tag{1}$$

The boundary conditions for a clamped circular plate:

$$w(r)=\frac{dw(r)}{dr}=0 \tag{2}$$

Using boundary conditions, trial solution can be simplified to: $w(r) = a_2(R^2 - r^2)^2$

Max. Displacement occurs at the Centre of plate (r =0)

$$w(r)_{\max}=\frac{Bd_o\left(R^2-r^2\right)^2}{64d_o-\left(32/21\right)BR^4} \tag{3}$$

Where, $$B=\frac{\epsilon_o V^2}{2Dd_o^2}$$

It is clear that W_{max} goes to infinity as $BR_4/42d_o$ approaches unity, which gives the limiting value of the voltage. *i.e.* Pull-in voltage, defined as max. Voltage applied at which upper membrane collapses with the lowest substrate.

$$V=\frac{9.16}{R^2}\sqrt{\frac{d_o^3 D}{\epsilon_o}} \tag{4}$$

For the constant case, the Galerkin's method gives the exact solution as-

$$w(r)=\frac{\epsilon_o V^2}{128Dd_o^2}\left(R^2-r^2\right) \tag{5}$$

The capacitance of the device at a given bias voltage is given by[3].

$$C=\frac{4\pi\epsilon_o}{21d_0}\sqrt{\frac{42M}{B}}\tan^{-1}\tan^{-1}\left(\sqrt{\frac{21}{32}}\frac{BR^2}{\sqrt{BM}}\right) \tag{6}$$

Where, $$M=(BR^4-42d_o)$$

Also, considering a uniform hydrostatic pressure of intensity q_0, the solution for combined loading is given by

$$w(r)=\frac{\left(\frac{q_o}{D}+B\right)d_o\left(R^2-r^2\right)}{64d_o-1.52BR^4} \tag{7}$$

Here, a constant hydrostatic pressure of 200 kPa is applied on the top surface of the plate and the deflection is determined for various bias voltages.

Formulation and Simulation for Square shaped membrane in CMUT

A schematic of an electrostatically actuated configuration composed of two parallel rectangular microplates is considered in this theoretical analysis. Its schematic is shown in Fig. 5 and parameters for simulation are shown in Table 2. The space between the two microplates is assumed as a vacuum or air with a dielectric constant ε_0. The deflection of the top micro-plate is assumed to be small compared to its thickness h^4.

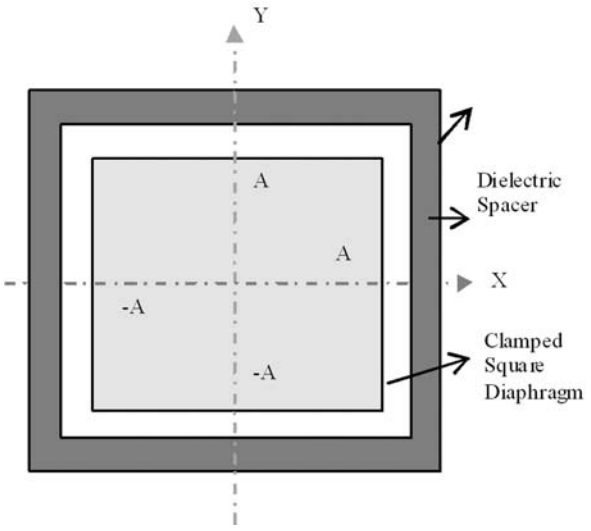

Fig. 2 Clamped Square

Table 2 – Parameters Used in Simulation

Parameters	Value
Length, 2*a*	40 μm
Thickness, *h*	1 μm
Young's Modulus, *E*	1.30×10^5 MPa
Poisson's ratio, *u*	0.28
Separation distance, *d*	0.2 μm
Dielectric constant, ε_o	8.85×10^{-12} F/m

For the transverse deflection *(w = w(x, y))* of the micro-plate under a distributed electrostatic force, the partial differential equation can be written as -

$$D\frac{\partial^4 w}{\partial x^4}+2\frac{\partial^4 w}{\partial x^2\partial y^2}+\frac{\partial^4 w}{\partial y^4}=F_e(x,y) \tag{8}$$

x and *y* are the coordinates originated at the center point of the micro-plate; *D* is the flexural stiffness. The classical thin micro-plate theory is used for the deflection analysis.

$$D=\frac{Eh^3}{12(1-u^2)} \tag{9}$$

Integrating the integrals and then solving the resulting equation for k_{00}-

$$d\int_{-b}^{b}\int_{-a}^{z}\nabla^4 w\times\varnothing_{00}\mathrm{dxdy}-\mathrm{k}_{00}\int_{-ba}^{ba}\int\nabla^4 w\times\varnothing_{00}^2 dxdy=Q_1$$
$$=Q_1\left(\int_{-b}^{b}\int_{-a}^{a}\varnothing_{00}dxdy+\frac{k_{00}}{d}\int_{-b}^{b}\int_{-a}^{a}\varnothing_{00}dxdy\right) \tag{10}$$

The resulting k_{00}, provides consistent solutions with the physical situation in which the deflection of the micro-plate increases with the applied voltage,

$$k_{00}=\frac{\left(3a^4+2a^2b^2+3b^4\right)d^2\pi^4-9a^4b^4Q_1-M}{\left(5a^4+4a^2b^2+5b^4\right)d\pi^4}$$

Where,

$$Q_1=\frac{\epsilon_0 V^2}{2dD} \tag{11}$$

The $w_{sq}(x,y)$ represents the transverse deflection of a clamped square micro-plate under electrostatic force; M_{sq} is given by-

$$w_{sq}(x,y)=\frac{84d^2\pi^4-9a^4Q_1-M_{sq}}{14d\pi^4}\cos^2\left(\frac{\pi x}{2a}\right)\cos^2\left(\frac{\pi y}{2a}\right)$$

\Where,

$$M_{sq}=\sqrt{64d^4\pi^8-592a^4d^2\pi^4Q_1+81a^8Q_1^2} \tag{12}$$

Results and Discussion

The parameters for study considered are deflection, capacitance, pull-in voltage and deflection profile for combined effect for hydrostatic and electrostatic forces.

Figure 3(a) shows the deflection in membrane with respect to change in voltage by Eq. (4) and Eq. (5), which is formed by considering linear term and constant term respectively. At moderate bias voltages, the difference between two plots is not significant but it becomes significant after bias voltage exceeds 60 V.

Figure 3(b) is plotted with the help of Eq. (12). Comparing Figures 3(a) and 3(b), it can be seen that pull-in voltage for circular plat occurs somewhere near 80 V while for square plate it occurs near 45 V. Thus square plate having lower pull-in voltage is considered much better than circular plate.

Figure 4(a) shows plot for bias voltages up to 60 V for circularplates. The graph is plotted with the help of

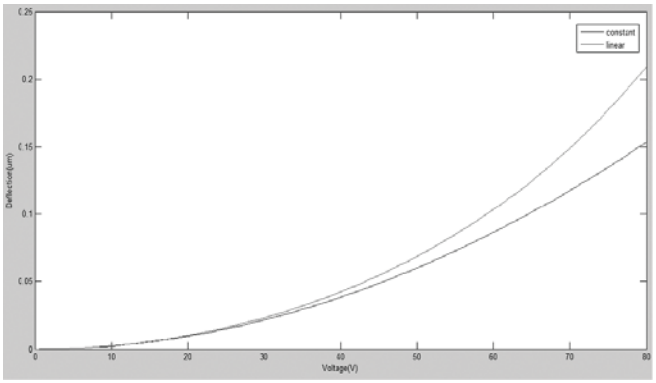

Fig. 3(a) Centre point deflection with respect to voltage for circular plates.

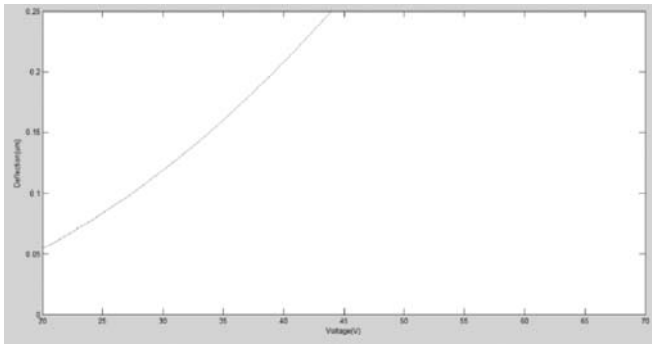

Fig. 3(b) Centre point deflections with respect to voltage for square plates.

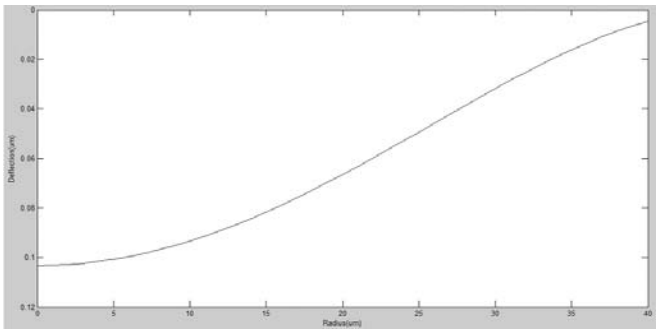

Fig. 4(a) Deflection with respect to radius at bias voltage of 60 V.

Eq. (3) and putting the value of V in B. Figure 4 (b) shows that at a DC bias of 80 V, the displacement of the centre found is 0.21um.

Figure 5 depicts the capacitance at different bias voltages for circular plates given by Eq. (6).

Figure 6 shows the deflection of the circular plate subjected to hydrostatic and electrostatic pressures both

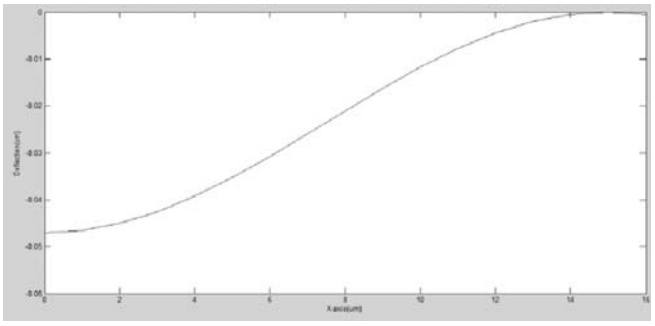

Fig. 4(b) Deflection profile with respect to radius at bias voltage of 60 V.

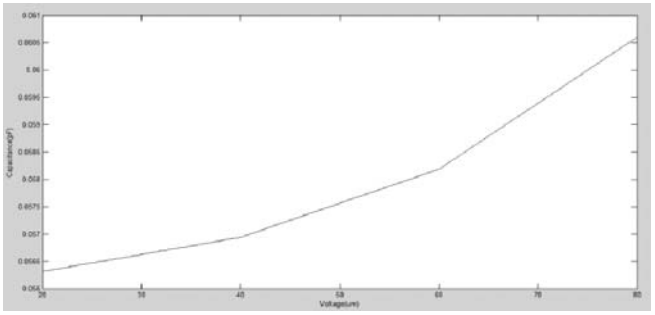

Fig. 5 Variation of capacitance with respect to bias voltage for circular microplate.

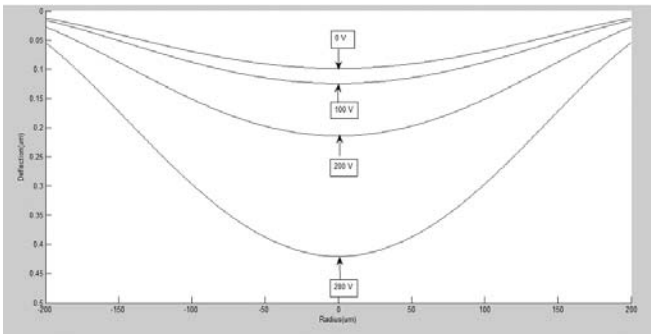

Fig. 6 Deflection profile for various bias voltages when a constant hydrostatic pressure of 200 kPa is applied on top surface of plate.

applied simultaneously at different bias voltages given by Eq. (7).

Figures 7(a) and 7(b) are also plotted by Eq. (12) by setting y=0 and x=0 respectively at bias voltage of 60V and 80 V.

Conclusion

The mathematical equations has been solved to study the difference in parametric changes of the circular and

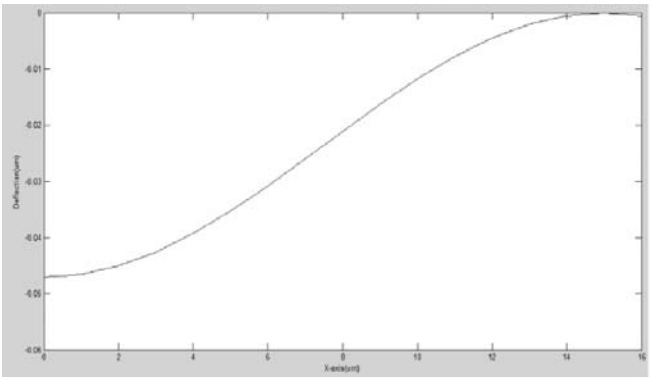

Fig. 7(a) Deflection profile with respect to x-axis at bias voltage of 60 V.

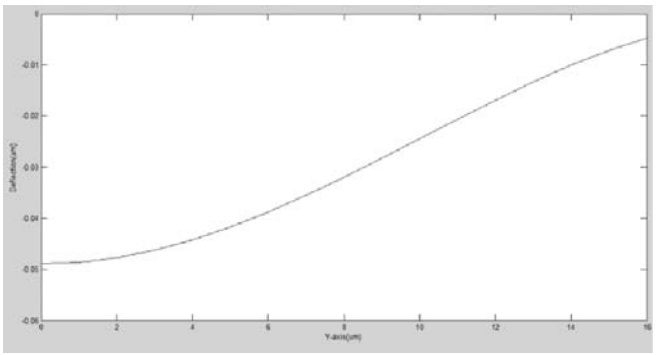

Fig. 7(b) Deflection profile with respect to y-axis at bias voltage of 80 V.

square plate CMUT's. In this paper, we compared the deflection and pull-in voltage for circular and square shaped micro-plate using Galerkin method. Also, the capacitance and hydrostatic pressue at various bias voltages for circular plate has been plotted. Circular membrane is often used in CMUT's as it generates lowest stress concentration and equalized electrostatic force in all directions. While, square membranes were reported to produce the maximum area efficiency of the device. This has been seen that the deflection of circular is better than the square micro plates.

References

1 **Hansen S.T., Mossawir B.J., Ergun A.S., Degertekin F.L**. and **Khuri-Yakub B.T.**, "Air-Coupled non-destructive evaluation using micromachined ultrasonic transducers," in Proc. *IEEE Ultrasonics Symp.* 2 (1999) 1037-1040.

2 **Ahmad B.** and **Pratap R.**, " Elasto-Electrostatic Analysis of Circular Microplates Used in Capacitive Micromachined Ultrasonic Transducers", *IEEE Sensors Journal,* 10(11) (2010).

3 **Sharma R., Agarwal R.** and **Arora A.**, "Performance Analysis of MEMS-Based Ultrasonic Transducer with Different Membrane Materials", *Recent Trends in Sensor Research and Technology,* **1**(3), ISSN:2393-8765.

4 **Li Z., Zhao L., Jiang Z., Ye Z., Dai L.** and **Zhao Y.**, " Mechanical behavior analysis on Electrostatically actuated rectangular microplate", *Journal of Micromechanics and Microengineering,* (2015).

J. Pure Appl. Ultrason. 38 (2016) pp. 76-79

Study of Lennard Jones potential repulsive term exponent, relative association and interaction parameter in binary liquid mixture at different frequencies

Ashok Kumar Dash[1] and Rita Paikaray[2]

[1]Department of Physics, Lokanath College, Korua, Patkura, Kendrapara-754134, India
[2]Department of Physics, Ravenshaw University Cuttack-753003, India
*E-mail: ashok.phy@rediffmail.com

The study of molecular interaction in organic liquid mixture plays an important role in the development of molecular science. The present investigation deals with the study of Lennard Jones potential repulsive term exponent, relative association and interaction parameter to explain molecular interaction in binary liquid mixture of an aprotic liquid dimethyl acetamide (DMAC) with isobutyl methyl ketone at different frequencies and at constant temperature 308K.The study of DMAC is important because of its utilization in industry and pharmaceuticals. Ultrasonic velocity (U) and density (ρ) of the binary liquid mixture at different frequencies 2 MHz, 4 MHz, 6 MHz and 8MHz have been measured at temperature 308 K. Lennard Jones potential repulsive term exponent (n) relative association (R_A) and interaction parameter (χ) have been calculated for the entire range of mole fraction and are interpreted to explain molecular interaction occurring in the liquid mixture.

Keywords: Binary mixture, ultrasonic velocity, mole fraction, relative association, interaction parameter.

Introduction

A large number of investigations have been made on the molecular interaction in liquid mixtures by various methods like ultraviolet, dielectric constant, infrared, Raman effect, nuclear magnetic resonance and ultrasonic methods. Presently, ultrasonic method is a powerful method to provide information regarding the physiochemical properties of liquid system[1-9]. Literature survey reveals that less work has been done on the molecular interactions in the mixtures of dimethyl acetamide.It is a dipolar solvent with high boiling point and good thermal and chemical stability and used as solvent in various solvent extraction processes. The study of Lennard Jones potential repulsive term exponent, relative association and interaction parameter in binary liquid mixture of dimethyl acetamide (DMAC) with isobutyl methyl ketone at different frequencies can be helpful to test suitability of the modifier for DMAC, which would increase the extraction efficiency of DMAC.

The physical and chemical properties of liquid mixture can be studied by the non-linear variation of ultrasonic velocity, Lennard Jones potential repulsive term exponent, relative association and interaction parameter with concentration in a liquid mixture.

Experimental

The liquid mixtures of various concentrations in mole fraction were prepared by taking chemicals of analytical grade (E Merck) which were used as such without further purification. The mole fractions were varied between 0.1 and 0.9 so as to have the mixture of different compositions. Liquid mixtures of different mole fractions were prepared on concentration scale with a precision 0.0001g using an electronic digital balance. Densitiy ρ of liquid mixture was determined by a specific gravity bottle of 10ml capacity[10,11]. The ultrasonic velocity U was measured by a multifrequency interferometer with a high degree of accuracy operating at different frequencies[12]. An electronically operated constant temperature water bath is used to circulate water through the double walled measuring cell made up of steel

containing the experimental liquid mixture at the desired temperature.

Theory and Calculation

Using the measured data Lennard Jones potential repulsive term exponent (n), relative association (R_A) and interaction parameter (χ) have been calculated from the following relations.

$$n = (6\ V_m / V_a) - 13 \quad (1)$$

Where $V_m = M/\rho$ = molar volume, $V_a = (M / \rho)\ [1 - (U/ U_\infty)]$ = available volume, M = molecular mass of the liquid mixture and $U_\infty = 1600$ m/s

$$R_A = (\rho / \rho_0)\ (U_0/ U)^{1/3} \quad (2)$$

Where ρ_0 and U_0 are density and ultrasonic velocity of DMAC respectively.

$$\chi = (U/U_{ideal})^2 - 1 \quad (3)$$

Where $U_{ideal} = X_1U_1 + X_2U_2$ = ideal mixing velocityof the liquid mixture.

Results and Discussion

The variation of density ρ, ultrasonic velocity U, molar volume V_m, available volume V_a with mole fraction of DMAC at 308 K for frequencies 2 MHz, 4 MHz, 6 MHz and 8 MHz for the binary liquid mixture are presented in Figs. 1-4 respectively. The variation of Lennard Jones repulsive term exponent n, relative association R_A and interaction parameter χ are given in Figs. 5 to 7.

The increase in density ρ with the increase in mole fraction of DMAC as shown in Fig. 1, indicates the presence of dipole-dipole interactions in the binary liquid mixture. The increase in ultrasonic velocity with the increase in mole fraction of DMAC as shown in Fig. 2

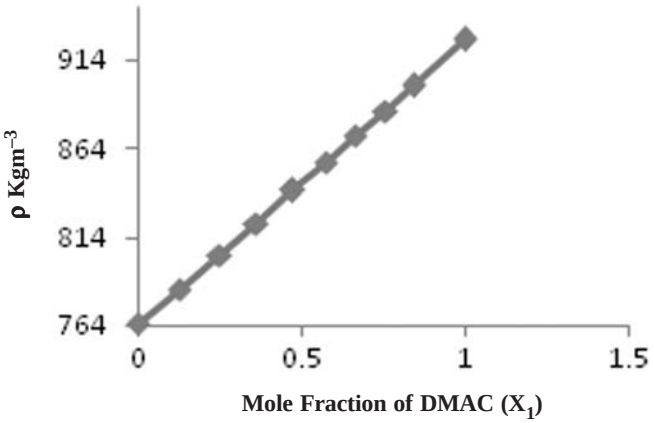

Fig. 1 Variation of ρ Versus X_1

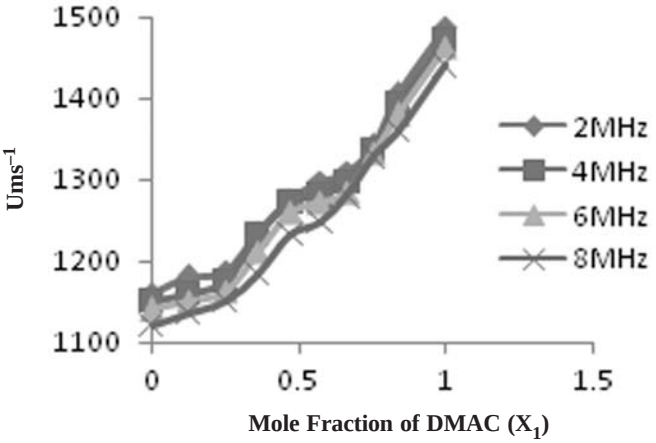

Fig. 2 Variation of U Versus X_1

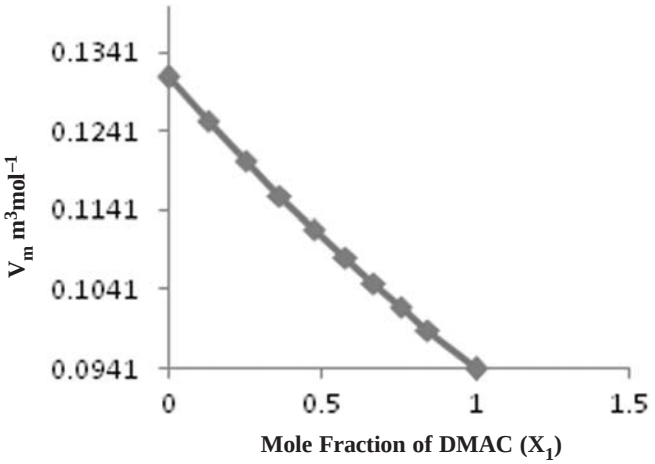

Fig. 3 Variation of V_m Versus X_1

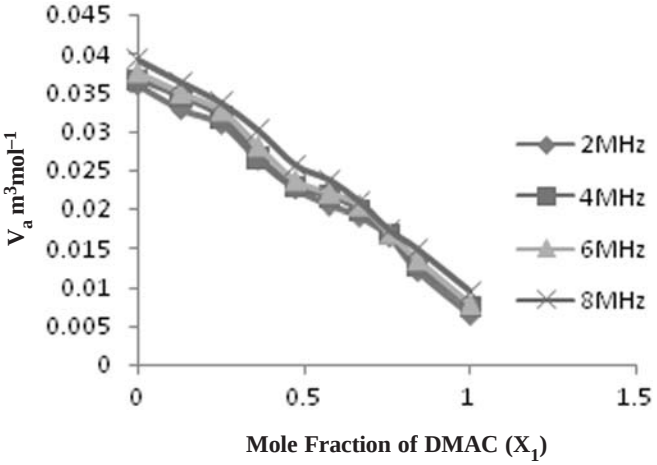

Fig. 4 Variation of V_a Versus X_1

at a particular frequency indicates increase in intermolecular forces in the binary mixture[13-15]. The variations of molar volume V_m and available volume V_a

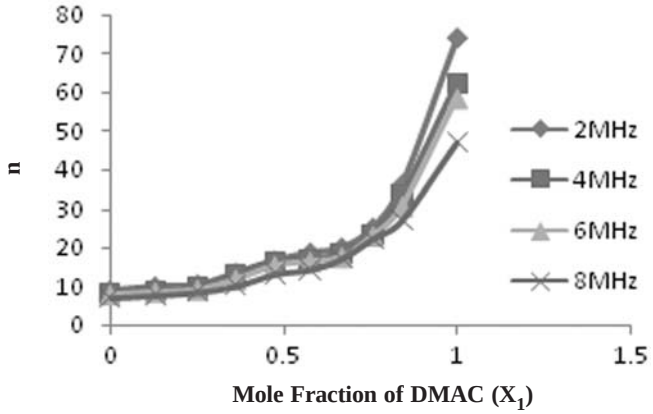

Fig. 5 Variation of n Versus X_1

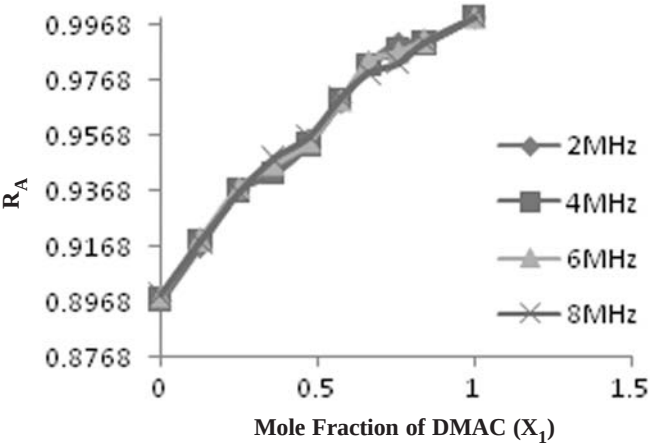

Fig. 6 Variation of R_A Versus X_1

with the increase in mole fraction of DMAC are depicted in Figs. 3 and 4. The decrease in molar volume and available volume is due to the net packing of molecules which may be due to the dipole-dipole interactions in the binary liquid mixture.

Lennard-Jones potential is given by the relation[16].

$$\varphi(r) = -Ar^{-6} + Dr^{-n}$$

Where *r* is the intermolecular distance, *n* is the Lennard-Jones potential repulsive term exponent and *A* and *D* are constants. The first term comes from attractive forces while the second term comes from repulsive forces. It is clear that larger the value of *n* smaller is the second term. Therefore large value of *n* indicates that the attractive forces are dominant over the repulsive forces. Fig. 5 shows that the values of *n* increase with the increase in concentration of DMAC which indicates the increasing dominance of attractive forces over repulsive forces in the liquid mixture. Further, the values of *n* decrease with the increase in frequency for a particular concentration which indicates the increase in repulsive forces resultin gdecrease in molecular interaction in the liquid mixture. This also explains the reason for the decrease in ultrasonic velocity with the increase in frequency[17].

It is observed from Fig. 6 that the values of relative association R_A increases with the increase in mole fraction of DMAC for all frequencies and this increase in relative association indicates the presence of the dipole-dipole interactions between molecules in the liquid mixture. Such increase of relative association also indicates that the liquid system is in a more compressed state and the component molecules are much closer to each other at higher concentration of DMAC.Relative association remains almost constant for all frequencies at a particular concentration.

Figure 7 shows that the values of interaction parameter χ are negative over the entire range of mole fraction of DMAC for frequencies 2 MHz, 4 MHz, 6 MHz and 8 MHz which indicate the existence of dispersion interactions in the binary liquid mixture. Further interaction parameter shows irregular trend with the change of frequency[18].

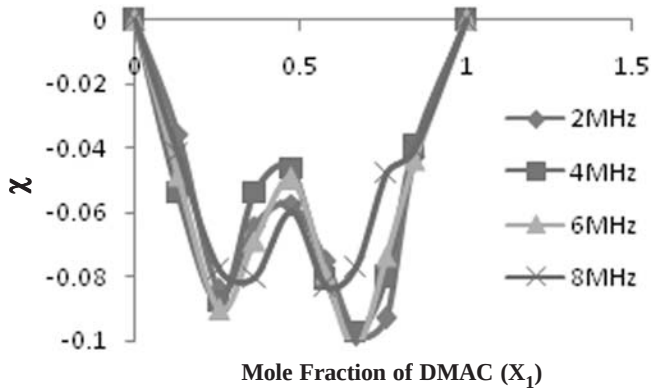

Fig. 7 Variation of χ Versus X_1

Conclusion

On the basis of the experimental values of density and ultrasonic velocity and computed values of Lennard Jones potential repulsive term exponent, relative association and interaction parameter it is concluded that there exists molecular association, dipole-dipole interaction and dispersive forces in the binary mixture of DMAC with isobutyl methyl ketone. The decrease in the values of Lennard Jones potential repulsive term exponent with the increase in frequency for a particular concentration of DMAC confirm the decrease in molecular interaction in the liquid mixture due to the increase in frequency.

Acknowledgements

One of the authors AKD is grateful to the UGC (ERO), Kolkata, India for providing financial support in the form of Minor Research Project grant.

References

1 **Kanappan V.** and **Santhi J.**, Ultrasonic study of induced dipole-dipole interactions in binary liquid mixtures, *Ind. J. Pure Appl. Phys.,* **43** (2005) 750-754.

2 **Dash A.K.** and **Paikaray R.**, Acoustical study on ternary mixture of dimethyl acetamide (DMAC) in diethyl ether and isobutyl methyl ketone at different frequencies, *Phys. Chem. Liq.,* **51**(6) (2013)749-763.

3 **Kubendram R., Liakat Ali Khan F., Asghar J., Aravinthraj M.** and **Udayaseelan J.**, Ultrasonic studies of N, N-dimethylacetamide and N-methylacetamide with alkoxyethanols in carbon tetrachloride at different temperatures, *Scho. Res. Lib.,* **3**(2) (2011) 568-576.

4 **Dash A.K.** and **Paikaray R.**, Ultrasonic Study on Ternary Mixture of Dimethyl Acetamide (DMAC) in Diethyl ether and Acetone, **1**(3) (2013) 12-20.

5 **Natrajan R.** and **Ramesh P.**, Ultrasonic velocity determination in binary liquid mixtures, *J. Pure Appl. Ind. Phys.,* **1**(4) (2011) 252- 258.

6 **Dash A.K.** and **Paikaray R.**, Molecular interaction studies in ternary liquid mixture of dimethylacetamide using ultrasonic technique at 308 K, *Phys. Chem. Liq.* **53**(2) (2015) 230-241.

7 **Bhatnagar D., Joshi D., Gupta R., Kumar Y., Kumar A.** and **Jain C.L.**, *Res. J. Chem. Sci.,* **1**(5) (2011) 6-13.

8 **Dash A.K.** and **Paikaray R.**,Visco Metric, Volumetric and Acoustic Studies in Ternary Mixture of Dimethyl Acetamide and Diethyl Ether in an Aprotic Solvent, *Int. J. Sc. Res.,* (2015) 5-9.

9 **Praharaj M.K., Mishra P.R., Mishra S.** and **Satapathy A.**, Study of thermodynamic and transport properties of ternary liquid mixture at different temperatures, *Pelagia Res Lib.* **3**(3) (2012) 1518-1530.

10 **Thirumaran S.** and **Rajeswari M.**, Acoustical studies on binary liquid mixtures of some aromatic hydrocarbons with dimethylsulphooxide (DMSO) at 303.15K, *Sch. Res. Lib.,* **2**(2) (2011) 149-156.

11 **Shanmuga Priya C., Nithya S., Velraj G.** and **Kanappan A.N.**, Molecular interactions studies in liquid mixture using ultrasonic technique, *Int. J. Adv. Sc. Tech.,* **189** (2010) 59-73.

12 **Dash A.K.** and **Paikaray R.**, Studies on Acoustic Parameters of Ternary Mixture of Dimethyl Acetamide in Acetone and Isobutyl Methyl Ketone using Ultrasonic and Viscosity Probes, *Int. J. Chem. Phys. Sci*., 3(4) (2014) 69-79.

13 **Dash A.K.** and **Paikaray R.**, Acoustical study in binary liquid mixture containing dimethyl acetamide using ultrasonic and viscosity probes, *Der Chem. Sin.,* **5**(1) (2014) 81-88.

14 **Palani R., Saravanan S.** and **Kumar R.**, Ultrasonic studies on some ternary organic liquid mixtures at 303, 308 and 313K Ultrasonic studies on some ternary organic liquid mixtures at 303, 308 and 313K, *RASAYAN J. Chem.,* **2**(3) (2009) 622-629.

15 Rajagopal K. and Chenthilnath S., Excess thermodynamic studies of binary mixtures of 2-methyl 2-propanol with ketones, *Ind. J. Pure. Appl. Phys.,* **48** (2010) 326-333.

16 **Gupta A.K., Kumar K.** and **Karn B.K.**,Ultrasonic studies of binary liquid mixtures of o-cresol with ethylmethyl ketone, acetone acetophenone and ethylacetate, *J. Ind. Council Chem.,* **26** (2009) 77-81.

17 **Dash A.K.** and **Paikaray R.**, Study of molecular interaction in binary liquid mixture of dimethyl acetamide and acetone using ultrasonic probe, *Adv. in Appl. Sci. Res.,* **4**(3) (2013) 130-139.

18 **Dash A.K.** and **Paikaray R.**, Ultrasonic Studies on Molecular Interaction in Ternary Liquid Mixture of Dimethyl Acetamide at Different Frequencies, *Int. J. Adv. Sci. and Tech.,* **66** (2014) 89-104.

J. Pure Appl. Ultrason. 38 (2016) pp. 80-83

Studies of acoustical parameters of N-benzothiazol-2-yl-3, 5-disubstituted pyrazolines in DMF-water at different frequencies

A.G. Gotmare*, A.S. Burghate and W.A. Wadhal

Department of Chemistry, Shri Shivaji Science College, Amravati-444602, India
Sant Gadge Baba Amravati University, Amravati-444602, India
*E-mail: gotmare.anuja@gmail.com

Density (ρ), ultrasonic velocity (u) of DMF-Water and components1-Benzothiazol-2-yl-3-(2-hydroxy-5-methyl phenyl)-5-(4-methoxy phenyl) pyrazoline (BHMPMPP), 1-Benzothiazol-2-yl-3-(2-hydroxy-5-methyl phenyl)-5-phenyl pyrazoline (BHMPPP) and 1-Benzothiazol-2-yl-3-(2-hydroxy-5-methyl phenyl)-5-(4-chloro phenyl) pyrazoline (BHMPCPP) in different concentrations of DMF-Water mixture have been determined at 303.15K temperature at 2MHz and 4MHz frequency range. Acoustical parameters such as Adiabatic Compressibility (β), Intermolecular free length (Lf), Acoustic Impedance (Z), Relative Association (R_A), Isothermal Compressibility (β_T), Thermal Expansion Coefficient (α), Interaction Parameters (χ), solvation number (Sn) and some other parameters have also been investigated from density and ultrasonic velocity of experimental data. The results are discussed on the basis of molecular interactions viz. solute-solute, solute-solvent interaction.

Keywords: Density, Ultrasonic velocity, Acoustical parameters, Molecular interaction, pyrazolines.

Introduction

Ultrasonic technique is one the sensitive technique to elucidate the interactions in binary mixtures to their components and also the physicochemical behavior of solutions[1-3]. By scientific and industrial point of view measurement of ultrasonic velocity is a noninvasive technique, used to determine thermodynamic relation between the molecules of compounds in suitable solvent and with liquid mixtures. Ultrasonic technique find applications in fundamental research, medicine, industry, defense *etc.*

Density and ultrasonic velocity are the physico-chemical properties used to determine composition of pure components and their mixtures in terms of intermolecular interactions[4-7].

Studies of ultrasonic parameters are applicable to determine the interactions of compounds. Here heterocyclic compounds *i.e.* N-Benzothiazol-2-yl-3,5-disubstituted pyazolines are taken for the investigation of ultrasonic parameters. Pyrazoline is the N-containing heterocyclic compound. Pyrazoline compounds shows versatile biological activities like antimicrobial[8-9], analgesic[10], antioxidant[11] *etc*. Physical parameters of it are also studied[12-13].

The present work deals with the study of acoustic parameters of N-Benzothiazol-2-yl-3,5-disubstituted pyrazoline in DMF-Water binary mixture in different concentration and frequencies (2 MHz and 4 MHz) at 293.15 K. The result areinterpreted on the basis of intermolecular interactions.

Experimental

Materials and methods

During experimentation, binary solvents of DMF and Water was used. DMF was of SD Fine grade. The double distilled water was used throughout experiment. The purity of DMF and Water was 99.6% and 99.4% respectively. The solute BHMPMPP, BHMPPP, BHMPCPP were synthesized. For the experimentation, observations taken were of density and velocity of sound. Densitometer of DMA 35 and ultrasonic interferometer at 2 MHz and 4 MHz with frequency fluctuation of ±0.02%. The interferometer have high frequency generator and a balance contech balance of accuracy

(±0.001 gm) was used for weighing purpose.

Results and Discussion

Determination of various ultrasonic parameters starts from determining the velocity of the solution. The expression used to determine ultrasonic velocity is

$$u = \nu \lambda$$

where, u = ultrasonic velocity & λ = wavelength

From the values of ultrasonic velocity, adiabatic compressibility (β) was calculated by using Newton-Laplace equation.

Intermolecular free length (L_f) gives idea about the intermolecular interactions between molecules, so to determine it following expression was used

$$L_f = K\sqrt{\beta}$$

Where, K = Jacobson Constant

The product of velocity and density in medium is the acoustic impedance ($Z = u\rho$) which was also determined.

The relative association (R_A) was calculated by using expression

$$R_A = \left(\frac{\rho}{\rho_0}\right)\left(\frac{u_0}{u}\right)^{1/3}$$

Where, ρ_0, ρ, u_0 & u are the density and ultrasonic velocity of solvent and solution respectively.

Isothermal compressibility (β_T) and thermal expansion coefficient (α) were also calculated[14].

Interaction parameter (χ) was used to determine interactions by using equation

$$\chi = \left(\frac{u}{u_{ideal}}\right)^{2\text{-}1}$$

Where, u and u_{ideal} velocity of solution and solvent.

Solvation number (S_n) also calculated to know the association of molecules.

The calculated values of all parameters are listed in Table 1-2 and figure of some parameters against mole fraction shown in Figs. 1-3. The velocity of the solution increases as concentration increases. The increase in velocity is directly proportional to the molecular weight of the solute. Hence lead to solute-solvent interaction. While increase in frequency 2 MHz to 4 MHz ultrasonic velocity also increases due to molecular interaction in

Table 1 – The values of adiabatic compressibility (β), intermolecular free length (L_f), acoustic impedance (Z) & relative association (R_A) in binary solvent mixture (DMSO, Dioxan, Acetone) + water at 303.15K.

Conc.	$\beta\times10^{-10}$	$L_f\times10^{-09}$ 2 MHz	Z	R_A	$\beta\times10^{-10}$	$L_f\times10^{-9}$ 4 MHz	Z	R_A
				BHMPMPP				
0.01	4.11841	5.7953	1539902.88	0.97437	4.22057	5.8667	1521152.16	0.97835
0.02	4.09096	5.7759	1545139.4	0.97339	4.18567	5.8424	1527558.8	0.97711
0.03	4.08557	5.7721	1546395.6	0.97353	4.09177	5.7765	1545223.2	0.97378
0.04	4.07485	5.7645	1548508.08	0.97323	4.03807	5.7385	1555543.2	0.97176
0.05	4.03237	5.7344	1556962	0.97199	3.99616	5.7086	1564000	0.97053
				BHMPPP				
0.01	4.14615	5.8148	1534272	0.97476	4.13772	5.8088	1534833.6	0.97443
0.02	4.11009	5.7894	1541066.68	0.97345	4.12470	5.7997	1538333.6	0.97403
0.03	4.06177	5.7553	1550364.4	0.97178	4.11550	5.7932	1540210.88	0.97390
0.04	4.05685	5.7518	1551463.2	0.97181	4.10216	5.7838	1542870	0.97361
0.05	4.01868	5.7247	1559132.4	0.97074	4.03890	5.7391	1555224.8	0.97155
				BHMPCPP				
0.01	4.10882	5.7885	1541540.32	0.97375	4.13602	5.8076	1536463.04	0.97482
0.02	4.10174	5.7835	1543028	0.96801	4.05235	5.7486	1552403.36	0.97174
0.03	4.09634	5.7797	1544283.52	0.97384	4.01868	5.7247	1559132.4	0.97074
0.04	4.08929	5.7747	1545772.2	0.97380	3.95811	5.6814	1571176.8	0.96852
0.05	4.07771	5.7666	1548201.6	0.97368	3.87932	5.6245	1587297.6	0.96562

Table 2 – The values of isentropic compressibility (β_T), thermal expansion coefficient (α), interaction parameter (χ) & solvation number (S_n) in binary solvent mixture (DMSO, Dioxan, Acetone) + water at 303.15K

Conc.	$\beta_T \times 10^{-15}$	$\alpha \times 10^{-4}$ 2 MHz	χ	S_n	$\beta_T \times 10^{-15}$	$\alpha \times 10^{-4}$ 4 MHz	χ	S_n
				BHMPMPP				
0.01	5.6013	1.0170	0.21517	37826.3332	5.7402	1.0232	0.17784	37816.8221
0.02	5.5638	1.0153	0.22320	18914.4898	5.6926	1.0211	0.18754	18909.8391
0.03	5.5559	1.0149	0.22443	12609.7958	5.5643	1.0153	0.21441	12608.9451
0.04	5.5411	1.0142	0.22753	9457.5089	5.4911	1.0119	0.23044	9457.6913
0.05	5.4826	1.0115	0.23995	7541.5147	5.4334	1.0093	0.24283	7541.6557
				BHMPPP				
0.01	5.6402	1.0187	0.20778	33686.7032	5.6288	1.0182	0.20216	33685.3959
0.02	5.5909	1.0165	0.21825	16514.3315	5.4326	1.0092	0.20583	16512.9320
0.03	5.5250	1.0135	0.23249	10939.0776	5.6022	1.0170	0.20736	10937.2956
0.04	5.5178	1.0132	0.23373	8107.3040	5.5794	1.0160	0.21196	8106.1214
0.05	5.4651	1.0107	0.24494	6486.3386	5.4926	1.0120	0.23044	6485.7236
				BHMPCPP				
0.01	5.5887	1.0164	0.21825	39995.7862	5.6256	1.0181	0.20216	39991.3829
0.02	5.5787	1.0159	0.22011	19366.5060	5.5115	1.0129	0.22673	19367.3644
0.03	5.5707	1.0156	0.22134	12956.5649	5.4651	1.0107	0.23663	12957.8780
0.04	5.5607	1.0151	0.22320	9683.4514	5.3824	1.0069	0.25529	9685.4780
0.05	5.5444	1.0144	0.22629	7737.1664	5.2747	1.0018	0.28040	774.2601

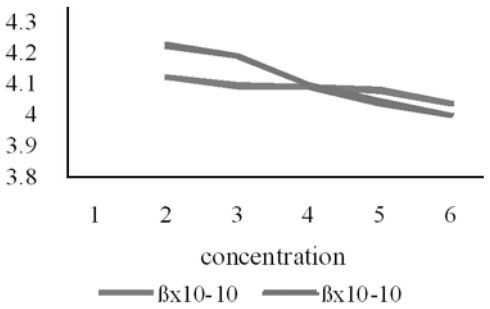

Fig. 1 Variations of adi. Compressibility with Mole fraction of binary mixture.

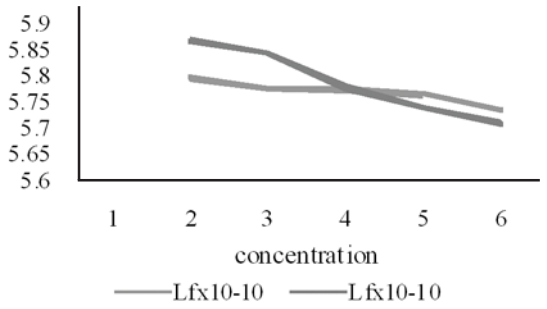

Fig. 2 Variations of intermolecular free length with Mole fraction of binary mixture.

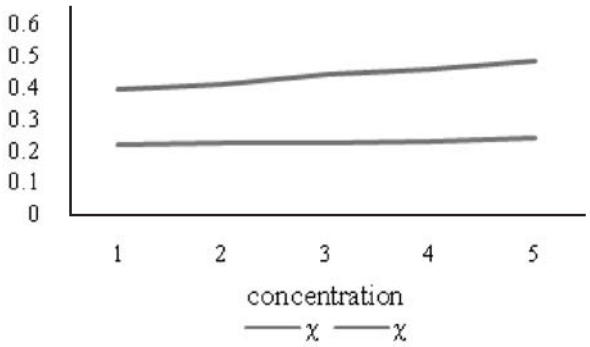

Fig. 3 Variations of interaction parameters with mole fraction of binary mixture.

liquid mixture.

The gradual decrease in adiabatic compressibility (β) with respect to increase in concentration suggest medium becomes more compressible. Intermolecular free length (L_f) give the idea about the interaction between existing components of the mixture.

Acoustic Impedance (Z) is the impedance offered to the sound wave by the components to the mixture whereas the relative association (R_A) is the measure of extent of association of components in the medium. The increasing trend in these parameters suggest the strengthening of interaction among the components. The interaction may be solute-solute, solute-solvent, solvent-solvent.

The interaction parameter (χ) values are found to be positive, positive values indicate the strong interaction between the binary mixture.

Conclusion

N-Benzothiazol-2-yl-3,5-disubstituted pyrazolines shows strong solute-solvent interaction with binary mixture solvent (DMSO, Dioxan, Acetone)-Water in two different frequencies at 303.15 K.

Acknowledgements

The authors are thankful to the principal of Shri Shivaji Science College, Amravati for giving permission and providing necessary facilities during the work.

References

1 **Punitha S.** and **Uvarani R.** ***et al.***, Physico-chemical studies on some saccharides inaqueous cellulose solutions at different temperatures- Acoustical and FTIR analysis *J. Saudi Chem. Soc.* **18** (2014) 657-665.

2 **Meshram Y.K.** and **Sonune K.N.** ***et al.***, Studies of Acoustic Properties of Substituted Heterocyclic Drugs in Dioxane & Dioxane-Water Mixture At 29°C. *Ind. J. Appl. Res.* **4**(7) (2014) 75-78.

3 **Sumathi T.** and **Maheswari J.U.** Ultrasonic and theoretical studies of some ternaryliquid mixtures at various temperatures. *Ind. J. Pure Appl. Phys.* **47** (2009) 782-786.

4 **Singh S.** and **Bahadur I.** ***et al.***, Density and speed of sound of 1-ethyl-3-methylimidazolium ethylsulphate with acetic or propionic acid at different temperatures. *J. Mol. Liq.* **199** (2014) 518-523.

5 **Gowrisankar M.** and **Venkateswarlu P.** ***et al.***, Ultrasonic Studies on Molecular Interactions in Binary Mixtures of N-Methyl Aniline with Methyl Isobutylketone, +3-Pentanone, and + Cycloalkanones at 303.15 KJ. Solution chem. **42** (2013) 916-935.

6 **Naik A.B.** Densities viscosities, speed of sound and some acoustical parameter studies of substituted pyrazoline compounds at different temperatures. *Ind. J. Pure Appl. Phys.* **53** (2015) 27-34.

7 **Naik A.B.** and **Narwade M.L.** ***et al.***, Molecular Interactions in SubstitutedPyrimidines-Acetonitrile Solutions at 298.15-318.15 K. *Russian J. Phy. Chem. A.* **88**(1) (2014) 37-41.

8 **Rani M.** and **Mohamad Y.** Synthesis, studies and in vitro antibacterial activity of some 5-(thiophene-2-yl)-phenyl pyrazoline derivatives. *J. Saudi Chem. Soc.* **18** (2014) 411-417.

9 **Shamsuzzaman** and **Khanam H.** ***et al.***, Synthesis, characterization, antimicrobial and anticancer studies of new steroidal pyrazolines. *J. Saudi Chem. Soc.* **20** (2016) 7-12.

10 **Sahu S.K.** and **Banerjee M.** ***et al.***, Synthesis, Analgesic, Anti-inflammatory and Antimicrobial Activities of Some Novel Pyrazoline Derivatives. *Tropical J. Pharmaceutical Res.* **7**(2) (2008) 961-968.

11 **Jois V.H.S.** and **Kalluraya B.** ***et al.***, Synthesis and antioxidant activity study of pyrazoline carrying an arylfuran/arylthiophene moiety. *J. Serb. Chem. Soc.* **79**(12) (2014) 1469-1475.

12 **Gotmare A.G.** and **Burghate A.S.** ***et al.***, Study of stability constants of complex of N-benzothiazol-2-yl-3, 5-disubstituted pyrazolines with some transition metal ions. *J. Chem. Pharma. Res.* **6**(12) (2014) 748-753.

13 **Burghate A.S.** and **Gotmare A.G.** ***et al.***, A Thermo dynamic and comparative study of complex formation of N-Benzothiazol-2-yl-3,5-disubstitutedpyrazolines with some transition metals by conductometry and pH-metry. *Int. J. Chem. Tech. Res.* **8**(11) (2015) 403-412.

14 **Venis A.R.** and **Rajkumar X.R**. Thermodynamic study on molecular interactions in ternary liquid mixture of morpholine, cyclohexanone and isoamyl alcohol at 308.15 and 318.15 K. *Asian J. Chem.* 24(3) (2012) 1195-1198.

J. Pure Appl. Ultrason. 38 (2016) pp. 84-87

Ultrasonic attenuation in terbium monophosphide

Vyoma Bhalla[1,2,*], Devraj Singh[2] and S.K. Jain[3]

[1]Amity Institute of Applied Sciences, Amity University, Noida-201303, India
[2]Department of Applied Physics, Amity School of Engineering and Technology, Bijwasan, New Delhi-110061, India
[3]Department of Applied Sciences, The NorthCap University, Sector 23A, Gurgaon-122017, India
*E-mail: bhallavyoma@gmail.com

The ultrasonic properties of terbium monophosphide have been investigated with its mechanical properties along <100>, <110> and <111> orientations. The second and third order elastic constants have also been calculated at 0K – 300K temperatures range using Coulomb and Born-Mayer potential. For finding the stability and ionic nature of TbP, some of the mechanical parameters have also been evaluated at room temperature. Additionally, thermal conductivity is also calculated using Slack's approach. Finally, ultrasonic attenuation in TbP is calculated. Obtained results of the present investigation are discussed in correlation with available results of previous findings.

Keywords: Terbium monophosphide, elastic properties, thermal conductivity, ultrasonic properties.

Introduction

Ultrasonic studies have been applied as an important tool for studying the microstructural features and inherent properties of different types of materials[1]. The rare-earth monopnictides have attracted the interests of numerous researchers due to their anomalous physical properties like magnetic, elastic, thermodynamics and phonon properties[2]. Buschbeck *et al*.[3] reported on the first magnetization measurements on TbP and TbSb in magnetic fields as high as 140 kOe covering the range from high to low temperatures. There are only few studies on TbAs and TbSb monopnictides. Nakanishi *et al.*[4] have examined the Fermi surface (FS) and magnetic properties of rare-earth monopnictide TbSb by means of de Haas-van Alphen (dHvA) and high-field magnetization measurements. Nakanishi *et al.*[5] have scrutinized the magnetic and elastic properties of rare-earth monopnictide TbSb by means of specific heat, high-field magnetization, and ultrasonic measurements. Ciftci *et al*.[6] presented thermodynamical, electronic and elastic properties of TbP using first principles method with plane-wave pseudopotential.

The TbP compound has not been studied very intensively and deeply using the first principle methods. Terbium monophosphide (TbP) is an intermetallic compound of simple rocksalt structure. After the discovery of the transition to type-II antiferromagnetism the magnetic and elastic properties of TbP have attracted considerable experimental and theoretical interest[7].

The aim of the present paper is to reveal elastic, mechanical and ultrasonic properties of TbP. The second and third order elastic constants (SOECs and TOECs) of TbP have been evaluated using Coulomb and Born-Mayer potential with two input parameters *i.e.,* nearest neighbor distance and hardness parameter. The SOECs and TOECs are applied to find out mechanical constants such as Young's modulus, shear modulus, bulk modulus, Poisson's ratio and tetragonal modulus of TbP. Further, SOECs and TOECs are used to compute ultrasonic properties such as ultrasonic velocity and attenuation along <100>, <110> and <111> directions. The thermal conductivity has been computed at room temperature.

Theory

The Coulomb and Born-Mayer type potential has been applied to find out the SOECs and TOECs, which follow Brugger's definition of elastic constants[8]. Leibfried *et al.*[9] developed anharmonic theory of lattice dynamics to find out elastic constants at different temperatures

obtained by addition of elastic constant at 0K and elastic constant at a particular temperature, *i.e.*,

$$C_{IJ}(T) = C_{IJ}^{0} + C_{IJ}^{vib}$$

and

$$C_{IJK}(T) = C_{IJK}^{0} + C_{IJK}^{vib} \quad (1)$$

C_{IJ} and C_{IJK} are the second and third order elastic constants. *'0'* and *'vib'* stands for 0 K and particular temperature such as 100 K, 200 K and 300 K respectively. The detailed expressions for temperature dependent SOECs and TOECs are given in our previous paper[10].

The expressions for finding the values of Young's modulus, bulk modulus, anisotropic shear modulus, tetragonal modulus, Zener anisotropy parameter, Poisson's ratio are given in our previous paper[11].

The ultrasonic velocities along <100>, <110> and <111> direction are of three type *i.e.* V_L, V_{S1} and V_{S2} (here L and *S* stand for longitudinal and shear modes of propagation). The Debye average velocity plays a key role to determine other important properties and is obtained with the help of Debye model .The expressions for finding ultrasonic velocities for longitudinal and shear modes of propagation and Debye average velocity are given in literature[12,13].

The minimum thermal conductivity[13] of the lattice along different crystallographic direction has been calculated at room temperature.

Theory of ultrasonic attenuation was initially developed by Akhieser[14]. Further this theory was modified by Bommel and Dransfeld[15] and finally by Mason[16]. The Mason's modified form has been used for determining ultrasonic attenuation, $(\alpha/f^2)_L$ for longitudinal wave and $(\alpha/f^2)_s$ for shear wave. The expressions to find out ultrasonic velocity and ultrasonic attenuation are given in our previous papers[17,18].

Results and Discussion

The SOECs and TOECs have been computed by means of two basic parameters *i.e.*, lattice and hardness parameter. The lattice constant[6] for TbP is 5.696 Å. The value of hardness parameter is taken as 0.313 Å for TbP. The computed values of temperature dependent SOECs and TOECs are given in Table 1. It is seen that the values of C_{11}, C_{44}, C_{111}, C_{166} and C_{144} increase with temperature while C_{12}, C_{112} and C_{123} decrease with temperature. The values of C_{456} remain constant. It is also observed that the values of elastic constants decreases with increase in molecular weight.

This type of behavior of higher order elastic constants is already found in other rare-earth materials like praseodymium monochalcogenides[17], lanthanum monochalcogenides[18] and rare-earth monoarsenides[19].

It is proposed that Cauchy relation[11] for SOECs and TOECs at 0K are:

$$C_{12}^{0} = C_{44}^{0}; C_{112}^{0} = C_{166}^{0}; C_{123}^{0} = C_{465}^{0} = C_{144}^{0} \quad (2)$$

The deviation of elastic constants in Table 1, suggest that the forces become more ionic with rise in temperature. The Cauchy's relation is followed at 0K but deviates at higher temperature due to vibrational part of energy.

The obtained results of SOECs and TOECs are applied to compute the Young modulus (*Y*), bulk modulus (*B*), shear modulus (*G*), tetragonal moduli (C_S), Poisson's ratio (σ), Zener anisotropy factor (*A*) and ratio *B/G*. These values are given in Table 2.

The Born criteria stability[6] is expressed as :

$$B = (C_{11} + 2C_{12})/3 > 0; C_{44} > 0$$
$$C_S = (C_{11} - C_{12})/2 > 0 \quad (3)$$

Table 1 – Temperature dependent SOECs and TOECs of TbP [in 10^{10} N/m^2]

Temp. [K]	C_{11}	C_{12}	C_{44}			
0	4.95	1.43	1.43			
100	5.21	1.44	1.35			
200	5.41	1.32	1.44			
300	5.63	1.28	1.45			
	C_{111}	C_{112}	C_{123}	C_{144}	C_{166}	C_{456}
0	–82.7	–5.81	2.40	2.40	-5.81	2.40
100	–84.4	–5.51	1.93	2.41	-5.85	2.40
200	–86.0	–5.31	1.77	2.42	-5.88	2.40
300	–87.8	–5.11	1.60	2.43	-5.91	2.40

Table 2 – Mechanical properties (in GPa) of TbP at room temperature.

B	Y	G	σ	B/G	C_S	A
27.3	42.3	17.1	0.241	1.60	21.8	0.663

It is obvious from Table 2 that the values of B, C_{44} and C_S are greater than 1. Thus, Born mechanical stability criterion has been satisfied by TbP. Hence, these are stable substances. The ratio of B/G (fracture/toughness) is less than 1.75 as given in Table 2. Thus, TbP are brittle in nature. The nature of bonding forces can be analysed from Poisson's ratio. For central forces, the value of Poisson's ratio should lie in the range $0.25<\nu<0.5$. For TbP considered in the present study, the value does not fall in this range which means that the forces are non central[26].

The values of ultrasonic velocities for longitudinal mode (V_L), shear modes (V_{S1} and V_{S2}), Debye average velocity (V_m) and Debye temperature (θ_D) are calculated using SOECs[10]. The values of these parameters are given in Tables 3–4.

In the chosen materials, the ultrasonic velocity for longitudinal mode is highest along <100> direction and minimum along <111> direction. This type of behavior has already been proved for other rare-earth materials[18, 19].

The computed values of thermal relaxation time, thermal conductivity and ultrasonic attenuation along different crystallographic directions <100>, <110> and <111> room temperature are presented in Table 4. The thermal relaxation time is of the order of picosecond. This indicates that these materials behave like intermetallics[20]. It also can be observed that the values of relaxation time decreases as we go from <100> to <111>. The values of ultrasonic attenuation is found lowest for TbP along <100> direction, where shear wave polarised along <100> direction and highest along <111>

Table 3 – Ultrasonic velocities V_L and V_S of TbP (all in the units of 10^3 m/s).

Temp	Ultrasonic velocities along different directions (at room temperature)						
	<100>		<110>			<111>	
	V_L	$V_{S1}=V_{S2}$*1	V_L	V_{S1}*2	V_{S2}*3	V_L	$V_{S1}=V_{S2}$*4
100	2.73	1.43	2.60	1.43	1.66	2.55	1.59
200	2.79	1.44	2.63	1.44	1.72	2.58	1.63
300	2.87	1.45	2.67	1.45	1.78	2.61	1.68
400	2.94	1.46	2.71	1.46	1.84	2.64	1.73
500	3.01	1.47	2.76	1.47	1.91	2.67	1.77

*1 Shear wave polarized along <100> direction; *2 Shear wave polarized along <001> direction
*3 Shear wave polarized along <110> direction; *4 Shear wave polarized along <110> direction

Table 4 – Thermoelastic attenuation $(\alpha/f^2)_{th}$, ultrasonic attenuation due to p-p interaction $(\alpha/f^2)_L$, $(\alpha/f^2)_S$ and $(\alpha/f^2)_S$ along <100> , <110> and <111> directions (all in $\times10^{-16}$Nps^2 m^{-1}), Debye average velocity, V_D (10^3 m/s), Debye temperature, θ_D (K) thermal relaxation time, τ (ps) and thermal conductivity (Wm^{-1}K^{-1}) TbP at room temperature.

Direction	$(\alpha/f^2)_{th}$	$(\alpha/f^2)_L$	$(\alpha/f^2)_S$	$(\alpha/f^2)_S$
<100>	0.0004	0.191	0.050	-
<110>	0.0017	0.241	0.879	0.038
<111>	0.0017	0.215	0.440	-
	V_D	θ_D	τ_{th}	κ
<100>	1.63	170.6	7.29	
<110>	1.75	183.8	6.28	1.965
<111>	1.84	193.1	5.69	

direction where shear wave polarized along <110> direction. It is also observed that ultrasonic attenuation due to p-p interaction for longitudinal wave is predominant over total thermal loss.

Conclusion

In the summary of present results, we conclude that TbP are stable as it follow Born stability criterion. Coulomb and Born- Mayer potential is applied successfully to evaluate higher order elastic constants for TbP. Investigated material is brittle in nature as it has ratio of fracture/toughness less than 1.75. On the basis of picoseconds order of thermal relaxation time for the chosen material we can say that TbP is of intermetallic character. The minimum attenuation along <100> direction reveals that it is most suitable direction for the anisotropic study of these materials. The obtained results of present investigation are useful for their future performance and further studies.

References

1 **Santos L.K., de Figueiredo J. J.** and **da Silva C.B.**, A study of ultrasonic physical modelling of isotropic media based on dynamic similitude, *Ultrasonics*, **70** (2016) 227-237.

2 **Natali F., Ruck B. J., Plank N. O., Trodahl H. J., Granville S., Meyer C.** and **Lambrecht W.R.**, Rare-earth mononitrides, *Prog. Mat. Sc.*, **58** (2013)1316-1360.

3 **Buschbeck A., Chojnowski C., Kötzler J., Sonder R.** and **Thummes G.**, Field-dependent phase transitions and magnetization of the type II-antiferromagnetsTbP and TbSb, *J. Magn. Magn. Mat.*, **69** (1987) 171-182.

4 **Nakanishi Y., Sakon T., Motokawa M., Ozawa M.** and **Suzuki T.**, De Haas-van Alphen study of the spin splitting of the Fermi surface in TbSb, *Phys. Rev. B.*, **69** (2004) 024412.

5 **Nakanishi Y., Sakon T., Motokawa M., Ozawa M., Suzuki T.** and **Yoshizawa M.**, Elastic properties and phase diagram of the rare-earth monopnictideTbSb, *Phys. Rev. B*, **68** (2003) 144427.

6 **Ciftci Y.O., Mogulkoc Y.** and **Evecen M.**, In: New Developments in Computational Intelligence and Computer Science, ISBN: 978-1-61804-286-6, Vienna (Austria) Marzo, INASE, (2015).

7 **Kötzler J., Raffius G., Loidl A.** and **Zeyen C.M.**, Singlet-ground state magnetism in TbP, Z. Physik B, *Cond. Matt.* **35** (1979) 125-132.

8 **Brugger K.**, Thermodynamic definition of higher order elastic coefficients, *Phys. Rev.*, **133** (1964) A1611-A1612.

9 **Leibfried G.** and **Haln H.**, Zurtemperatur-abhängigkeit der elastischenkonstanten von alkalihalogenidkristallen, *Z. Phys.*, **150** (1958) 487-525.

10 **Bhalla V., Singh D.** and **Jain S.K.**, Mechanical and Thermophysical properties of cerium monopnictides. *Int.J. Thermophys.*, **37** (2016) 33 (17 pp.).

11 **Bhalla V., Kumar R., Tripathy C.** and **Singh D.**, Mechanical and thermal properties of praseodymium monopnictides: an ultrasonic study, Int. J. Mod. Phys. B.27(2013) 1350116.

12 **Kittel C.**, *Introduction to solid state physics*, 8th ed., John Wiley & Sons, Inc. New Delhi, ISBN 047141526X (2005).

13 **Bhalla V.** and **Singh D.**, Anisotropic assessment of ultrasonic wave velocity and thermal conductivity in ErX (X: N, As), *Indian J. Pure Appl. Phys.*, **54** (2016) 40-45.

14 **Akhieser A.**, On the absorption of sound in solids, *J. Phys.* (USSR), **1**(1939) 277-287.

15 **Bömmel H.E.** and **Dransfeld K.**, Excitation and attenuation of hypersonic waves in quartz, *Phys.Rev.*, **117** (1960) 1245-1251.

16 **Mason W.P.**, Physical Acoustics, III B Academic Press, New York, (1965).

17 **Yadav R.R.** and **Singh D.**, Effect of thermal conductivity on ultrasonic attenuation in praseodymium monochalcogenides, *Acoust. Phys.*, **49** (2003) 595-604.

18 **Yadav R.R.** and **Singh D.**, Ultrasonic attenuation in lanthanum monochalcogenides. *J. Phys.Soc. Jpn.*, **70** (2001) 1825-1832.

19 **Bhalla V., Singh D., Jain S. K.** and **Kumar R.**, Ultrasonic attenuation in rare-earth monoarsenides, *Pramana*, **86** (2016) 1355-1367.

20 **Singh D.** and **Pandey D.K.**, Ultrasonic investigations in intermetallics, *Pramana*, **72** (2009) 389-398.

PhD Thesis Summary

Ultrasonic Non Destructive Testing Characterization of Condensed Materials

(Awarded 2016 by NIMS University, Jaipur, Rajasthan to Shivani Kaushik, DIET, Gurgaon)

This thesis is a theoretical study for the characterization of materials having NaCl-type structure. For characterization of the materials, its elastic behaviour and mechanical properties are analyzed. Since propagation of ultrasonic waves through a medium is the characteristic of the medium, the ultrasonic velocity and attenuation coefficient for the waves give the idea about the thermophysical properties of the material. This thesis is a theoretical study where higher order elastic constants and other constants governing the mechanical properties like-bulk modulus, shear modulus, Young's modulus, tetragonal moduli, anisotropic ratio and Poisson's ratio etc are computed theoretically. Various other parameters like ultrasonic velocity, Debye average velocity, Debye temperature, Grüneisen parameter, thermal conductivity, thermal relaxation time, acoustic coupling constant and ultrasonic attenuation are calculated. The second and third order elastic constants are computed using the Coulomb and Born-Mayer potential by using two basic parameters- hardness parameter and nearest neighbour distance. The obtained results are compared with the experimental and theoretical results available in literature. All the calculations are done in the temperature range 0-300K and along the three crystallographic directions <100>, <110> and <111> for the chosen materials.

The thesis comprises of six chapters. Chapter 1 deals with introduction to ultrasonics, properties of ultrasonic waves and its application in various fields. The significance of elastic constants and different modes of propagation and ultrasonic parameters like ultrasonic velocity, Debye temperature, Grüneisen parameter, thermal conductivity, nonlinearity parameter, thermal relaxation time and various types of attenuation are discussed. Chapter 2 is Review of Literature depicting various studies related to the materials and methods under study. Chapter 3 describes the material used and methods employed. The materials under study were monobismuthides of B, Cm and U; Berkelium monopnictides (BkN, BkP, BkAs, BkSb); Silver halides (AgCl, AgBr); Neptunium monopnictides (NpN, NpP, NpAs, NpSb). Chapter 4 describes the results obtained. The calculation of SOEC and TOEC; mechanical parameters like bulk modulus(B) *etc*, the values of ultrasonic velocities along different directions; Breazeale's nonlinearity parameter, values of Grüneisen parameter; specific heat capacity and energy density, thermal conductivity and thermal relaxation time; acoustic coupling constant for longitudinal(DL) and shear (D_s) waves along the three crystallographic directions <100>, <110> and <111>; variation of thermal attenuation with temperature and attenuation due to p-p interaction are tabulated in this chapter separately for all the chosen materials. Chapter 5 is the discussion of obtained results. Chapter 6 is the summary and conclusion.

It can be said that the results obtained gave a comparison about the mechanical and thermal properties of the materials under study in the selected temperature range and along different crystallographic directions. The materials were found to be mechanically stable, anisotropic and semi-metallic in nature. The attenuation caused by p-p interactions dominated over the thermal attenuation in the selected temperature range. This is in agreement with the Mason-Bateman approach to evaluate ultrasonic attenuation. So it can be said that this approach can be successfully applied to semi metallic compounds.

The results of this thesis can be beneficial for scientists working in the field of material characterization and engineering while applying these materials for various purposes.

Journal of Pure and Applied Ultrasonics

INFORMATION FOR AUTHORS

1. Type of Contribution

JOURNAL OF PURE AND APPLIED ULTRASONICS welcomes contributions on all aspects of ultrasonics including ultrasonic studies in medical ultrasonics, NDT, underwater, transducers, materials & devices and any other related topic. Contributions should fall into one of the following classes.

Paper - These should be on original research work contributing to scientific developments. They should be written with a wide readership in mind and should emphasize the significance of the work.

Reviews and Articles - Includes critical reviews and survey articles.

Research and Technical notes - These should be short descriptions of new techniques, applications, instruments and components.

Letters to the editor - Letters will be published on points arising out of published articles and papers and on questions of opinion.

Miscellaneous - Miscellaneous contributions such as studies, interpretive and tutorial articles, conference reports and news items are also accepted. Recommended contribution lengths are: Papers 2000-4000 words. Reviews and Surveys 2000-5000 words; Conference Reports 500-1500 words; News Items, Research and Technical Notes up to 1000 words.

2. Manuscripts

Manuscripts should be typed on one side of the paper in double spacing with wide margins on A4 size paper. The originals of text and illustrations plus two copies should be provided to facilitate the process of reviewing. Complete manuscript in MS WORD or Page Maker would ensure no mistake. Floppy containing article should be sent along with the manuscript.

Title - Titles should be short and indicate the nature of the contribution.

Abstract - An abstract of 100-200 words should be provided on the title page of paper and review article. This should indicate the full scope of the contribution and include the principal conclusions.

Mathematics - Mathematical expressions should be arranged to occupy the minimum number of lines consistent with clarity e.g., $(x^2+y^2)/(x-y)^{1/2}$.

Illustration - The line illustrations along with captions should be clearly drawn with black Indian ink. Figures in Excel are preferred.

References - References should be referred to in the text by number only. The reference number should be given as superscript. The corresponding reference shall contain the following information in order; names and initials of author (s)(bold), title of the work, journal or book title (italic), volume number (bold), year of publication in brackets, page number, e.g., **Giri R. and Nath G.,** Ultrasonic study of solvent extractant in nuclear technology, *J. Pure Appl. Ultrason.,* **37** (2015) 44-47.

Units and Abbreviations - Authors should use SI units wherever possible.